university of groningen / faculty of mathematics and natural sciences / biomedical engineering

Dosimetric validation of sCT images created from CBCT and MR images by a DCNN for the use of adaptive proton therapy in head and neck cancer patients.

Bas A. de Jong
S2608669

Department of Radiotherapy
University Medical Centre Groningen (UMCG)
The Netherlands

period: 11/02/2019-04/08/2019

Master's project

supervisor: Assoc. Prof. A.C. Knopf, UMCG, Department of Radiotherapy

mentor: dr. ir. A.T.M. Willemsen, UMCG, Department of Nuclear Medicine.

Dosimetric validation of CBCT based and MR based synthetic CT images created by a DCNN for the use of adaptive proton therapy in head and neck cancer patients.

Abstract

Adaptive proton therapy refers to the possibility to adjust treatment plans during the course of fractionated treatment to compensate for changes in patient anatomy. This insures sufficient treatment of the tumor while minimizing damage to surrounding organs at risk (OARs). In current clinical practice, adaptive proton therapy relies on computed tomography (CT) images. CT images are linked to imaging dose and thus the imaging frequency has to be well balanced. Cone beam computed tomography (CBCT) and magnetic resonance (MR) imaging are an alternative to CT imaging and can give a daily representation of the patient anatomy. However these images are not directly suited for proton dose calculations.

In this work, a Deep Convolutional Neural Network was trained and used to create synthetic CT (sCT) images based on CBCT and MR images. The aim of this research is to evaluate and compare the accuracy of proton dose distributions calculated on sCT images based on CBCT and MR images by a Deep Convolutional Neural Network (DCNN), for the use of adaptive proton therapy in head and neck cancer patients.

The quality of the sCT images was assessed by calculating mean absolute error (MAE) values for the sCT images, with respect to corresponding CT images. Geometric accuracy of the reconstruction of bony structures is assessed using the Dice similarity coefficient (DSC).

Dose distributions were calculated on sCT images and corresponding CT images using clinical treatment plans for 9 head and neck cancer patients. The accuracy of the proton dose calculations on sCT and corresponding CT images is compared and evaluated using gamma analysis and evaluation of the dose in clinically delineated organs at risk (OARs).

Average MAE values were found of 37 $\pm$ 4 HU and 58 $\pm$ 4 HU respectively for sCT images based on CBCT and MR images respectively. The Gamma analysis resulted in average pass rates of 98.6 $\pm$ 1% and 97.5 $\pm$ 1% for dose distributions calculated on sCT images created from CBCT and MR images, respectively. Furthermore, evaluation of dose volume histograms for the planning treatment volume (PTV) and OARs, showed that sCT images based on CBCT as well as on MR images are suitable for proton dose calculations, with avarage dose differences of less than 1%. From the results of this research we conclude that both sCT images based on CBCT and MR images could be suitable for the use in adaptive proton therapy for head and neck patients.

The use of sCT images for adaptive proton therapy enables daily evaluation of the impact of anatomical changes on the treatment. Furthermore, it simplifies workflows making the acquisition of repeated CTs (rCTs) along the treatment redundant.

Contents

1 Introduction

1.1 Radiotherapy

Every year approximately 110.000 Dutch citizens are diagnosed with a invasive tumor. About 3100 of these patients are head and neck cancer patients [1]. Treatment for these patients can involve surgery, chemotherapy, hormonal therapy and radiotherapy. In curative radiotherapy, the aim is to administer a high dose to a target volume, while maintaining the dose to surrounding healthy tissue as low as possible. By doing so, the goal is to kill the tumor cells and cure the disease, while keeping the side effects of the therapy to a minimum.

In this study we look at head and neck cancer patients. The head and neck cancer patient group is a group which is expected to benefit from proton therapy [2, 3]. And the head and neck patients were among the first patients treated at the proton treatment facility in Groningen. An important side effect in radiotherapy for head and neck cancer patients is dry mouth called xerostomia, caused by deterioration of the function of salivary glands [4]. Patients who suffer from xerostomia are prone to develop dental problems such as xerostomia related caries and demineralization of teeth [5, 6]. Furthermore, xerostomia can cause a burning sensation in the mouth and make swallowing and talking difficult [7, 5]. These side effects have a big influence on the quality of life of head and neck patients after radiotherapy, therefore efforts to reduce these side effects need to be made [4].

1.2 Treatment modalities

Radiotherapy can be performed using multiple modalities. A radiation dose can be administered by introducing a radiation source into the body of the patients at the site of the tumor, which is done in brachytherapy and molecular radiotherapy. Brachytherapy makes use of radioactive seeds or objects, which are placed inside or near the tumor and is used in for example the treatment of prostate and cervix tumors [8]. Molecular radiotherapy uses radiopharmaceuticals, which are introduced to the patients body by means of injection or ingestion. Tumors are targeted by using the chemical and biological properties of the radiopharmaceuticals [9]. Iodine-131 is a commonly used radiopharmaceutical for the treatment of thyroid cancer [10].

Another way of administering a radiation dose to a target is by the use of radiation beams in what is called external beam radiotherapy. Different radiation types are used within external beam radiotherapy. Photon beams with photon energies in the range of 50-500 keV are used to treat superficial tumors with a depth of upto 6 cm and photon energies in the range of 4-25 MeV are used to irradiate targets located deeper within the patients body [12, 11]. As individual photons travel trough the body, they only undergo a low amount of interactions and they might even pass trough without interacting entirely.

This is a consequence of the relatively low interaction probability of high energy photons with tissue. A photon beam is attenuated as it passes trough the tissue of the patient. This results in the deposition of a radiation dose along the path of the beam both in front of and behind the target volume [14].

Electron beams with energies in the range of 4-18 MeV are used to treat superficially located tumors with depths of up to 5 cm [13]. The interaction probability for electrons in tissue is much higher than for photons. Electrons undergo many scatter interactions over large angles as they travel trough tissue, creating a tortuous 'zig-zaggy' path and a more superficial deposition of the dose [14, 15].

A modality which has seen large innovation in resent years is to use particle radiation beams of ionized atomic nuclei, such as protons or carbon ions to irradiate a target volume [16, 17, 18]. Similar to electrons, the interaction probability for these charged particles is high, which causes many interactions along the path of the particles. The mass of the particles is much greater, for protons about 1833 times, compared with the mass of the electron. When colliding with the electrons in tissue, because of this large mass difference, the high energetic particles are scattered over small angles.

The large amount of interactions with small scattering angles, cause the high energetic particles to gradually deposit their energy along a roughly straight path in the tissue. When the particles have lost almost all their energy, the interaction probability increases and a higher amount of energy per unit length is deposited, which creates the characteristic bragg peak [14, 19]. If the particles are given the right amount of energy at the start, they will have lost all their energy after arriving at the planned spot in the target volume, and almost no dose is deposited behind this position. A graph of dose deposition as a function of depth for the different external beam radiotherapy modalities is shown in Figure 1 [20].

1.3 Adaptive proton therapy

Proton therapy enables the administration of highly conformal dose distributions to clinical targets, spearing the surrounding healthy tissue, and therewith reducing side effects [21, 22]. Highly conformal dose distributions however do impose problems, as treatment plans can become more sensitive to uncertainties, such as motion and changes in the patients anatomy. These changes affect the range of the protons and thereby the location at which they deposit their energy. When these effects are not sufficiently taken into account, they can result in under dosage of the target volume, and/or high dose to organs at risk (OAR) near the target volume.

Different strategies to mitigate the effects of changes in anatomy and target motion exist. Robust treatment planning can be employed to ensure sufficient treatment of the target volume [23, 24]. respiratory-gating or breath-hold strategies can be used to minimize motion effects [25, 26]. Dose calculations based on images taken throughout the treatment course can be used to trigger plan adaptations accounting for anatomical changes in what is called adaptive proton therapy (APT) [27, 28].

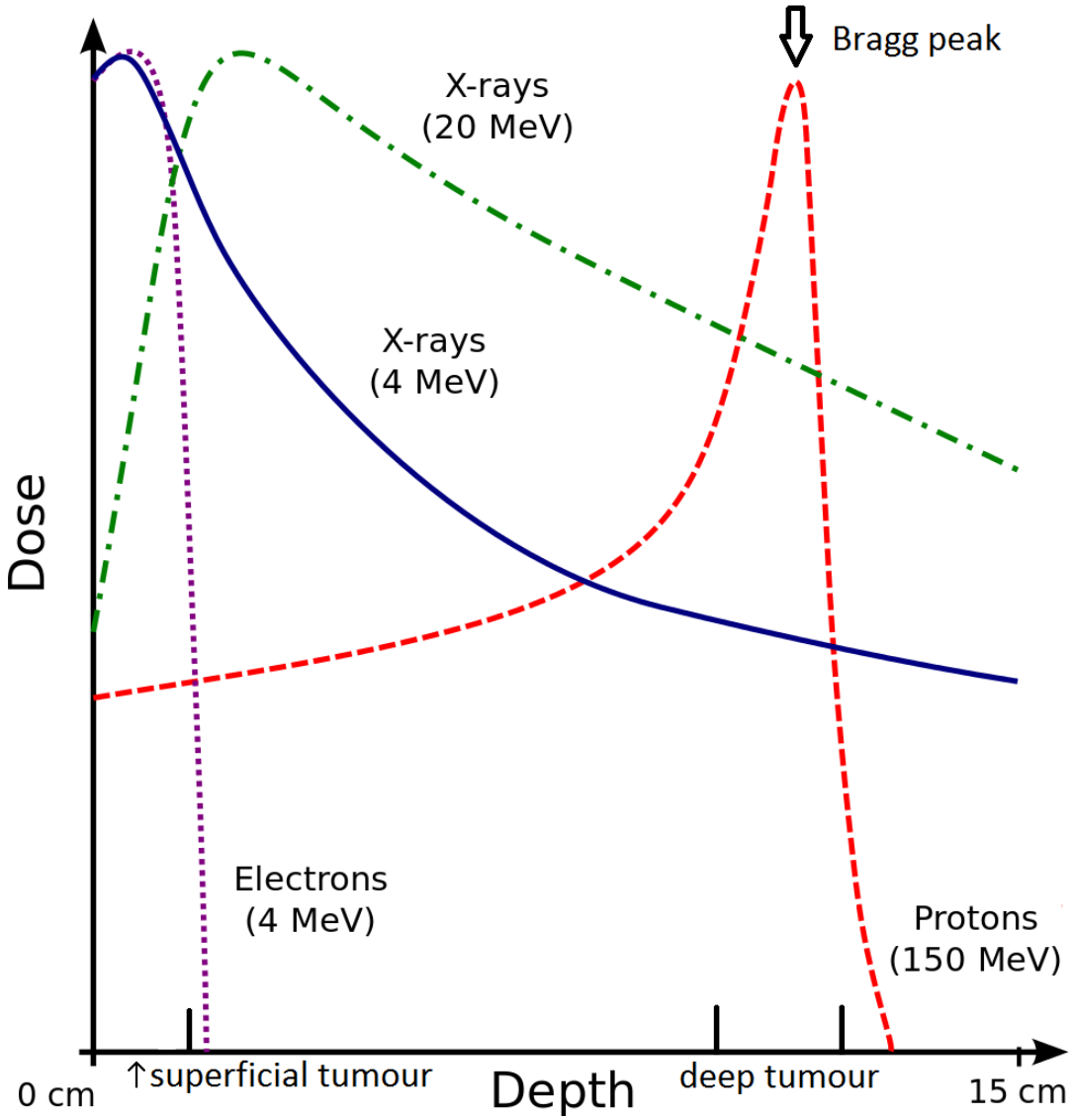

Figure 1: Dose depth curves for different external beam radiotherapy modalities [20].

During the course of radiotherapy treatment multiple imaging modalities can be used to get a representation of the patient anatomy. In current clinical practice, MR and planning CT (pCT) images are acquired before the start of the treatment, CBCT images are typically acquired before each treatment fraction, and the acquisition of repeat CT (rCT) images are scheduled about once a week. Examples of MR, CBCT and CT images are shown in Figure 2. MR images provide superior soft tissue contrast allowing optimal delineation of relevant targets and OARs [29]. The pCT yields information on the electron density, used for proton dose calculations. CBCT and rCT images are used for patient positioning verification and to evaluate anatomical changes.

The use of multiple imaging modalities does come with disadvantages. Extra imaging raises the costs of treatment and increases the clinical workload [30]. Inaccuracies in co-registration of MR to pCT images results in the need for increased planning margins [31, 32]. Acquiring CBCT, pCT and rCT images comes at the cost of a imaging dose for the patient [33, 34, 35].

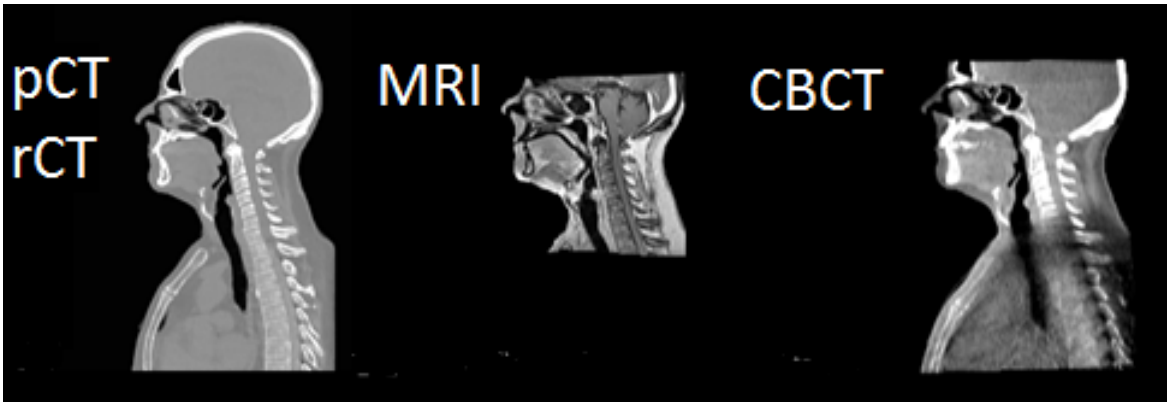

Figure 2: Examples of from left to right CT, MR and CBCT images of the same patient.

Currently, when significant changes in anatomy are observed in the CBCT image a rCT image has to be taken for recalculation and evaluation of the dose distribution, which can eventually lead to plan adaptation. This workflow is complicated and often prohibits the implementation of adaptive workflows. Clinical implementation of adaptive proton therapy would be much more realistic, if daily acquired CBCT images could be used for dose re-calculations, and if the treatment evaluation steps could be more automatized. In photon radiotherapy an alternative to daily CBCT imaging is daily MR imaging as available at combined MR-linac systems [36, 37]. In the future, also combined MR-proton systems might be realized [38, 39]. For these combined MR-proton machines, adaptive proton therapy workflows would be the ideal use case.

In addition to enabling smoother adaptive workflows, benefits of using CBCT images for sCT generation are the readily availability of the images, as they are made before each treatment fraction for various indications and the absence of geometric distortions, which can be present in MR images [40]. Benefits of using MR-images for sCT generation for adaptive workflow include, the high soft tissue contrast, which allows more accurate eval-

uation of OARs[41] and the lack of imaging dose received by the patient in the acquisition of MR images.

1.4 Synthetic CT used for APT

However, neither MR nor CBCT images by themselves are suitable for proton dose calculations. CBCT images have to low image quality [42, 43, 44] and the MR signal is not directly related to electron density information needed for proton dose calculation [45]. To overcome these issues multiple efforts have been made, to create artificial or synthetic CT (sCT) images based on CBCT and MR images suitable for proton dose calculations. Examples of different sCT creation methods are density override approaches, [46, 47, 48] atlas-based [48, 49, 50, 51] and voxel-based methods [52, 53].

In density override approaches, structures such as bone, soft tissue and air in the original images are segmented, and average CT values are assigned to the structures. Disadvantages of the density override approaches are that they are less accurate than other methods, as a single CT HU value is assigned to the whole structure, while CT HU values vary in structures and delineation of structures is not straight forward [48].

Atlas based methods use a database of CBCT or MR images with corresponding CT images. The atlas CBCT or MR images are registered and parts are matched onto the patients CBCT or MR image, the same transformations are performed on the atlas CT images and from this the sCT image is formed [49]. A disadvantage of atlas based methods is that they are quite computationally expensive with sCT generation times varying between minutes and hours,[54] and they typically deal worse with patients with large anatomical abnormalities [55].

Voxel based methods use statistical methods and fitting of models to predict voxel values on a local scale [54]. Voxel based methods often need multiple MR sequences which increases acquisition time [56]. An overview of methods for sCT generation from MR images has recently been made by Johnstone et al. [54].

Resent developments in deep learning have created new possibilities in image processing. One of the possibilities is to train a Deep Convolutional Neural Network (DCNN) to make the translation of a certain medical image type into an artificial different image type [58]. Using a DCNN sCT images can be generated from CBCT or MR images.

In this work a DCNN is used to generate sCT images based on CBCT and MR images (see Figure 3) The suitability of CBCT- and MR-based sCTs for adaptive proton therapy is tested in a head and neck patient cohort. The suitability for adaptive proton therapy is tested by recalculating a clinical proton plan on the sCT images and compare the resulting dose distributions with the original dose distribution, by using gamma analysis and evaluating of dose volume histogram (DVH) points in relevant OARs. To our knowledge, this is the first work comparing the feasibility of CBCT based and MR based adaptive proton therapy for the same cohort of patients.

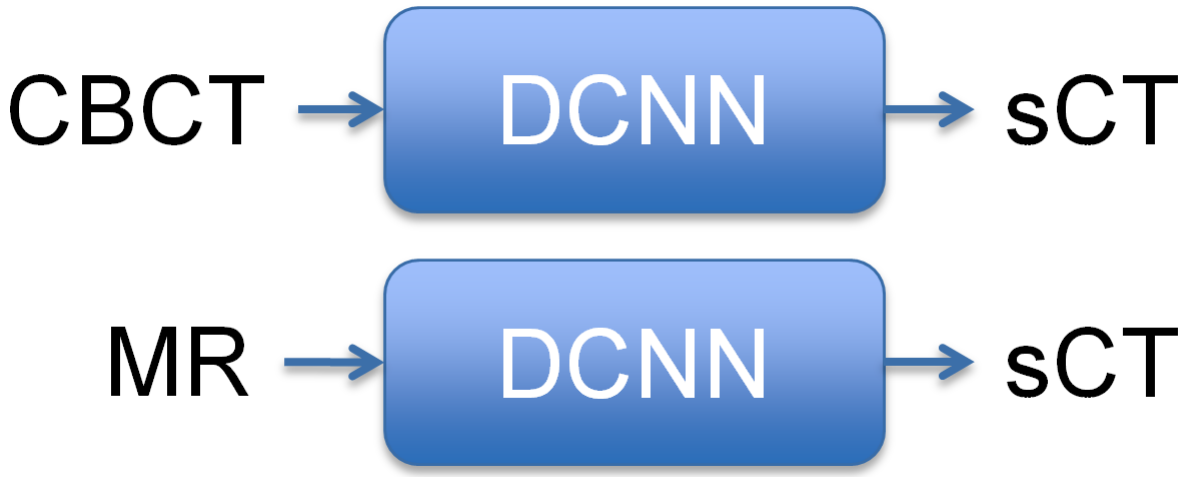

Figure 3: Flow chart of two pathways of generation of sCT images based on CBCT and MR images using a DCNN.

2 Methods

2.1 Neural network

The sCT images were created using a DCNN, a network architecture first used by X. Han for this task [58]. The DCNN which was used in this work was developed at the medical engineering group of Italian University Magna Graecia in Catanzaro [59]. Convolution filters can be represented by a three by three matrix containing numbers called weights in it. The weights indicate how the pixel values in a image which is convoluted are multiplied and added up. If the right weights for the convolution filter are chosen, the filter can detect features in the image. In the Laplace filter, the center pixel is multiplied by eight and the eight surrounding pixels are subtracted.

When an image is convolved with the Laplace filter, the output contains higher intensity pixels at locations where there was intensity change in the original image. The higher intensity pixels in the output image therefore effectively show edges in the original image. An example of the application of a Laplace convolution filter is shown in Figure 4 [57].

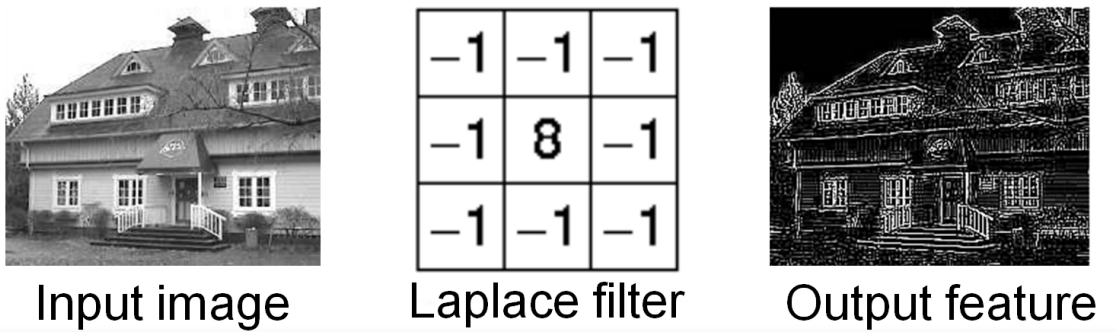

Figure 4: From left to right: input image, Laplace convolution filter, Output feature map [57].

The network consists of a encoding path, in which features at decreasing resolution are detected by means of an increasing number of three by three convolution filters. Features are identified at each resolution level in the encoding path and are reported to the same resolution level in the decoding path. In the decoding path the features from different resolutions are combined and a sCT image is gradually reconstructed to in the end get a high resolution sCT image as output. Figure 5 shows a graphical representation of the DCNN architecture used by X. Han [58].

The DCNN we used contained 27 convolution layers, four downsampling 'Max Pooling' layers, and four up-sampling 'Unpooling' layers. Similar to the network proposed by X. Han, our DCNN is a 2D DCNN, in the sense that it converts individual 2D CBCT or MR image slices to sCT image slices and stacks the converted slices afterwards to get the 3D sCT image volume.

At the start of the training, the network contains 32 million randomly initialized parameters or weights. The weights are optimized in a training procedure using MR- or CBCT- with their corresponding CT images. A loss function computes the difference between the sCT image generated by the network and the corresponding CT image. The weights are changed in small steps by gradient decent of the loss function, in a process called back propagation. As loss function, the mean absolute error (MAE) within the external contour of the patient was calculated using formula (1):

$$MAE = \frac{1}{N}\sum^{N}(|sCT_{ijk} - CT_{ijk}|) \tag{1}$$

in which N are the number of voxels within the external contour of the patient, sCT_{ijk} and CT_{ijk} are the voxel values at the same position in the image matrix within the sCT and corresponding CT image respectively.

The amount of data available for the training was artificially increased by using data augmentation in the form of small translations and mirroring of the image pairs. The batch size for the training was one, corresponding to individual 2D image slice pairs.

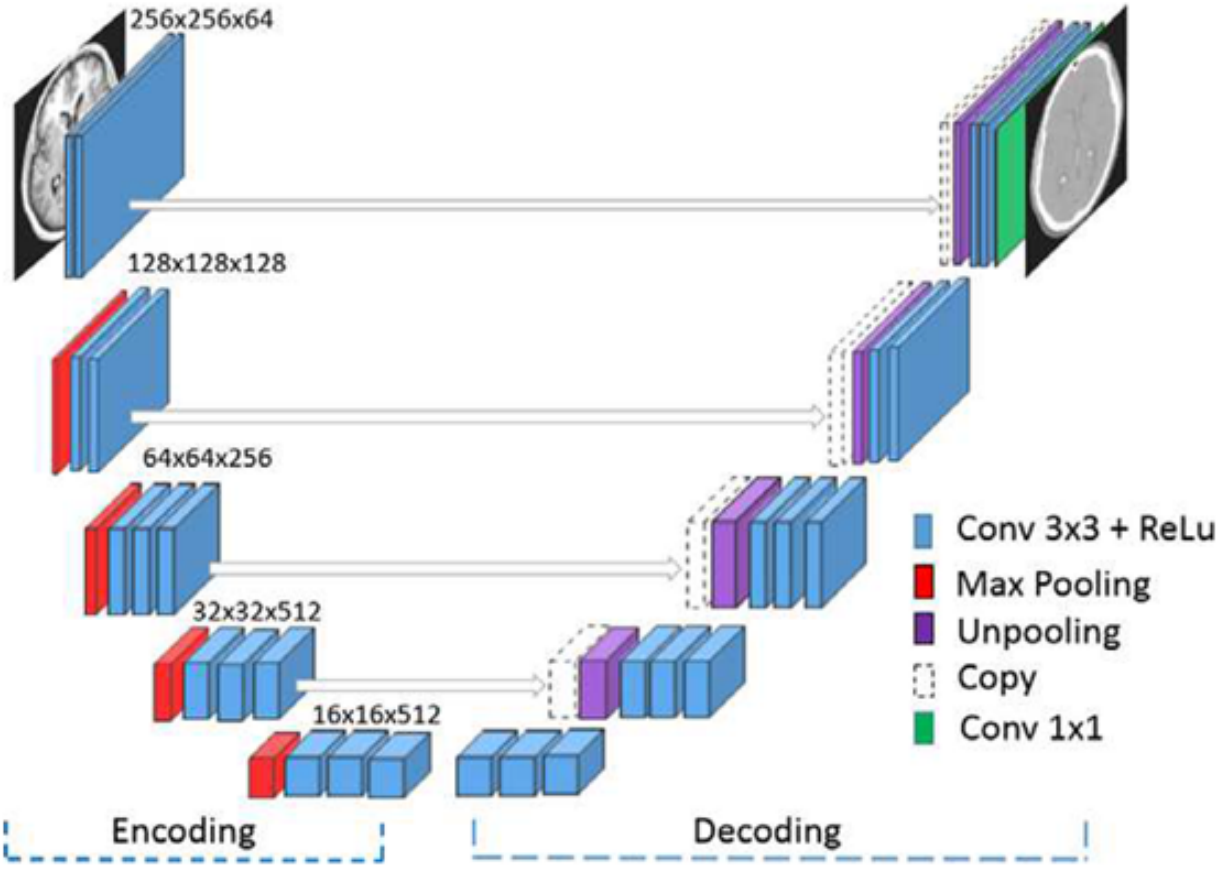

Figure 5: Graphical representation of U-net DCNN architecture proposed by Xiao Han for converting MR images into sCT images [58].

To enhance performance, three networks were trained to convert images of 3 orthogonal views, by using only either axial, sagittal or coronal slice pairs to train the network. The generated 2D sCT slices are stacked to get the 3D sCT image volume for each view. Subsequently, the resulting 3D sCT image volumes generated for each view were combined and averaged to get the final sCT image. By doing so context from different directions in the images is used to estimate sCT voxel values.

The patient population was divided into a training subset of 16 patients, validation of training subset of 2 patients and a testing subset 9 patients. Training of the networks was stopped when the loss for the validation subset did not decrease for five successive epochs. The optimized weights resulting in the lowest validation loss were then used to convert CBCT and MR images from the testing subset into sCT images.

MEA values between sCT created from MR images and corresponding CT images for the head and neck region calculated inside an external contour have recently been reported of 200.2 ± 23 HU and 90.7 ± 12.1 HU for a bulk density override and atlas-based method respectively [60]. For sCT's based on CBCT and MR images created using deep learning Generative Adversarial Networks, MEA values have been reported of 29 ± 5 and 47 ± 11 HU for brain radiotherapy patients, respectively [61, 62].

2.2 Data

Images of 27 head and neck proton therapy patients were used. The average age of the 27 patients was 62 years, with the oldest patient being 79 and the youngest 27 years old. 19 of the patients were male and 8 female. The MR and corresponding pCT image and the CBCT and corresponding rCT image of the patients were all made within 48 and 24 hours respectively, all in treatment position using a treatment mask.

The close-in-time acquisition of imaging pairs is required to assure a minimal amount of anatomical variations. A minimal amount of anatomical variations in the image pairs is a prerequisite for a successful DCNN training. The CBCT with rCT image pairs and MR with pCT images pairs were used for training the DCNN. To be able to compare the sCT images created based on CBCT with ones based on MR to the same corresponding CT image, both the CBCT and MR images were registered to the pCT images before they were converted to sCT images. An overview of which images are used for each part of this research is shown in Figure 6.

The pCT and rCT images were acquired using a Siemens SOMATOM Definition AS at 120 kV with a voxel size of 2X0.98X0.98mm. The CBCT images were acquired for position verification in a IBA proton treatment room at 100 kV with a voxel size of 2.5X0.51X0.51mm. CBCT imaging systems for proton therapy have only recently become available in 2014. The geometry of a CBCT setup for proton therapy is different from CBCT-setups used for photon therapy in CBCT linac combinations. The source to imager distance (SID) and source to axis distance (SAD) for proton therapy CBCT setups are

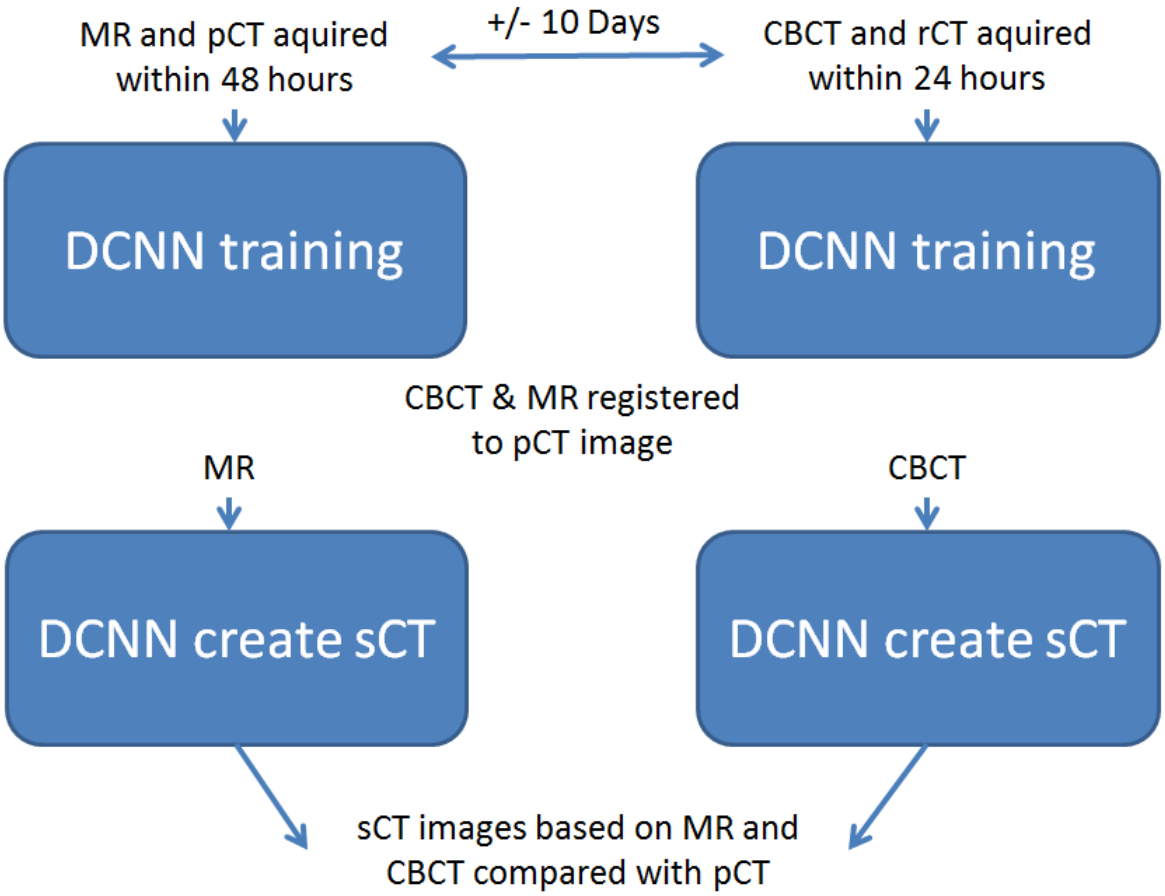

Figure 6: Overview of images used in the different parts of the research.

usually larger.

For our system the SID and SAD were 3470 mm and 2875 mm respectively. In CBCT linac systems typical values for SID and SAD are 1500 mm and 1000 respectively. An advantage of these higher distances is a decrease in the fraction of scattered photons reaching the detector. Disadvantages of the higher distances are, the need of a higher tube current to reach the same photon flux at the detector. Furthermore, maintaining correct alignment with respect to the isocenter could be more difficult, which is important for the image quality [63].

Acquisition of the MR images was performed after a single dose of gadoterate meglumine (0.2 ml /kg). A 3D dual-echo spoiled gradient recalled (SPGR) sequence was acquired on a 3T Siemens Skyra system to obtain two series of both out-phase (OP) and in-phase (IP) images with echo times of 2.38 and 4.76 ms respectively and TR 5.5 ms; FA 9 degree; voxel size 0.9 mm isotrope and bandwidth 455 Hz per pixel of which only the in-phase image was available.

2.3 Data preparation

To train the DCNN, deformable co-registration of CBCT with corresponding rCT images and MR with corresponding pCT images is necessary to get as close to voxel wise alignment as possible. First the co-registration process of the CBCT with rCT and subsequently the co-registration process of MR with corresponding pCT images will be discussed.

2.3.1 CBCT training data

Training data preparation for the CBCT images was performed by Adrian Thummerer, PhD student at the department of Radiotherapy at UMCG. External masks were created for the CBCT and rCT images. Automatic segmentation involving thresholding and closing image operations in the software tool Plastimatch were used to create the masks. Every mask was checked and residual holes were manually filled. The treatment couch and mask were cropped from the CBCT image, by keeping the data within the external mask, and setting the voxels outside the external mask to -1000 HU, corresponding to the CT HU value of air. The same steps were also performed to crop the treatment couch and mask from the rCT image.

Rigid registration of the masked CBCT to rCT images was performed in Plastimatch. After the initial registration, masks from CBCT and rCT were combined and used to only preserve overlapping data. Furthermore, CBCTs and corresponding rCTs were cropped at the shoulders, because of the limited field of view(FoV) and poor image quality of CBCTs in the area below (see Figure 7).

A diffeomorphic Morphons deformable image registration algorithm, implemented in openREGGUI, an open source registration toolbox for Matlab, was utilized to register

the cropped CBCT to the cropped rCT images. This algorithm was previously used and tested for deformable image registration of CBCT to CT images in the head and neck area. The image pairs of registered CBCTs and rCTs were subsequently used to train the DCNN.

To allow a comparison of MR- and CBCT-based sCTs above steps were repeated to register the original CBCT also to the pCT, which were subsequently converted to sCT by the trained DCNN.

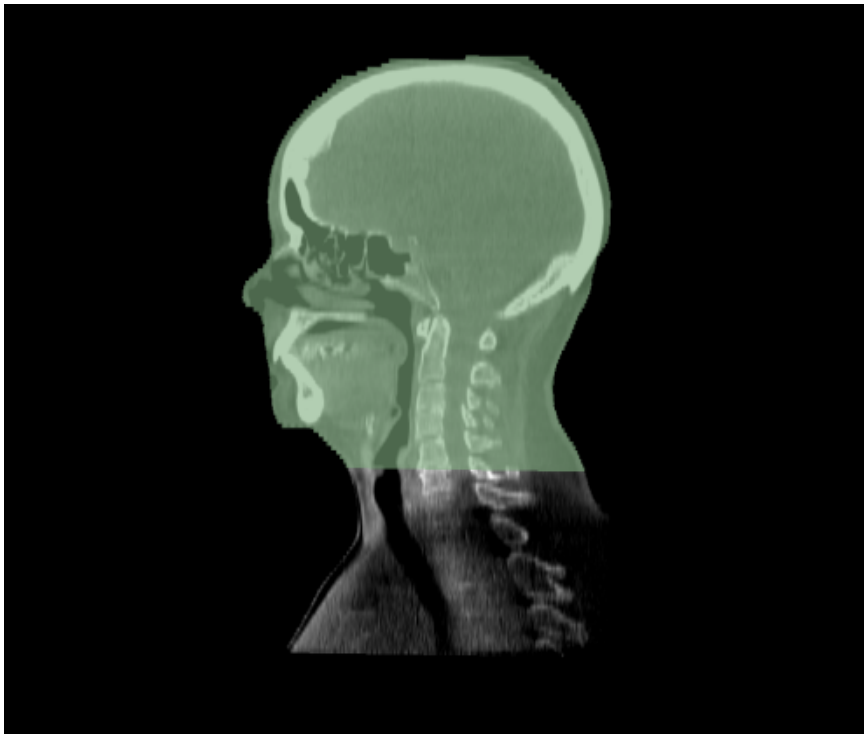

Figure 7: Example of a CBCT image. The part of CBCT image used for training of the network is coloured green.

2.3.2 MR training data

External masks were made for the MR and pCT images using thresholding followed by closing image operations in Plastimatch. Manual filling of residual cavities in the masks was performed in 3D Slicer. The MR and pCT images were masked using the external masks, by doing so, the immobilization mask and treatment table are cropped from the images to only leave the patient volume. The voxel values in the volume outside the external masks were set to -1000 HU and 0 corresponding to the value for air in the pCT and MR images respectively.

The MR images were corrected for magnetic field bias, reducing the low frequency noise in the images using plastimatch. The MR and pCT images only had a small overlapping volume at the start of the co-registration process. To initialize the co-registration,

the center of gravity of external masks of the MRI and pCT image were matched and the transformation was applied to the MR images using Plastimatch.

A rigid registration was used to further align the images, and deformable registration was used to correct for residual small differences in patient posture and positioning using Elastix software [64, 66, 67]. A visualization of a deformation vector field for the deformable registration can be seen in Figure 8.

Because of the multi-modal nature of the data, mutual information was used as metric for the co-registration [68]. The deformable registration was based on parameter file par0002 from the Elastix database and included a bending energy penalty, to decrease unrealistic deformations of the image [64]. The deformable registration parameter file can be found in appendix B.

The co-registered MR and pCT images were re-sampled to the average size of the pCT images to get a consistent matrix size for the whole dataset. Finally the re-sampled MR and pCT images were masked using the Boolean intersection of the external masks of the MR and pCT images, this was done to only keep overlapping data, while again setting the voxel values outside the combined mask to the value of air. The data preparation steps for MR can be seen in Figures 9 and 10 The scripts used for processing of the MR data for training of the network can be found in appendix A1 and A2.

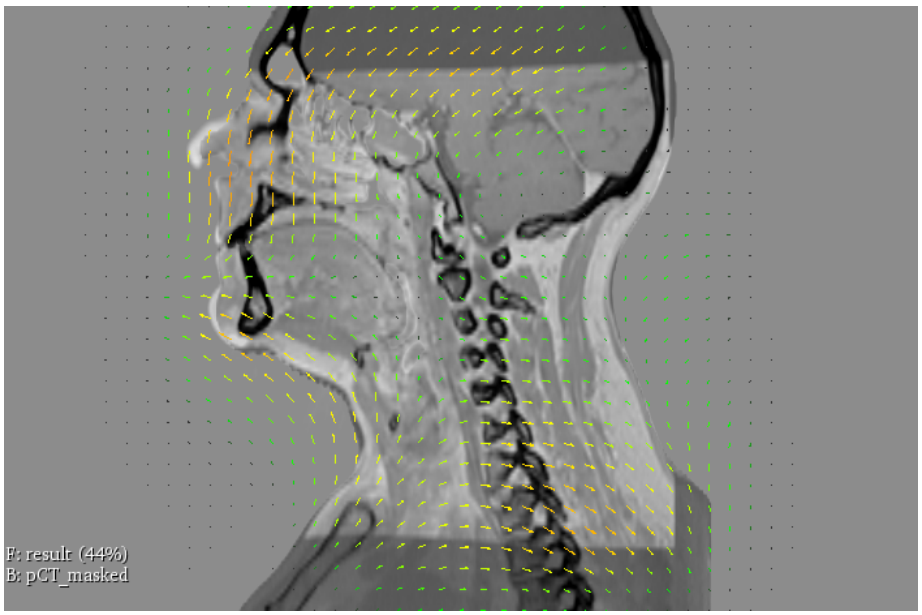

Figure 8: Visualization of deformable registration vector field on top of MR- and inverted pCT image overlay. Length of deformation vectors was multiplied by two, to improve visibility.

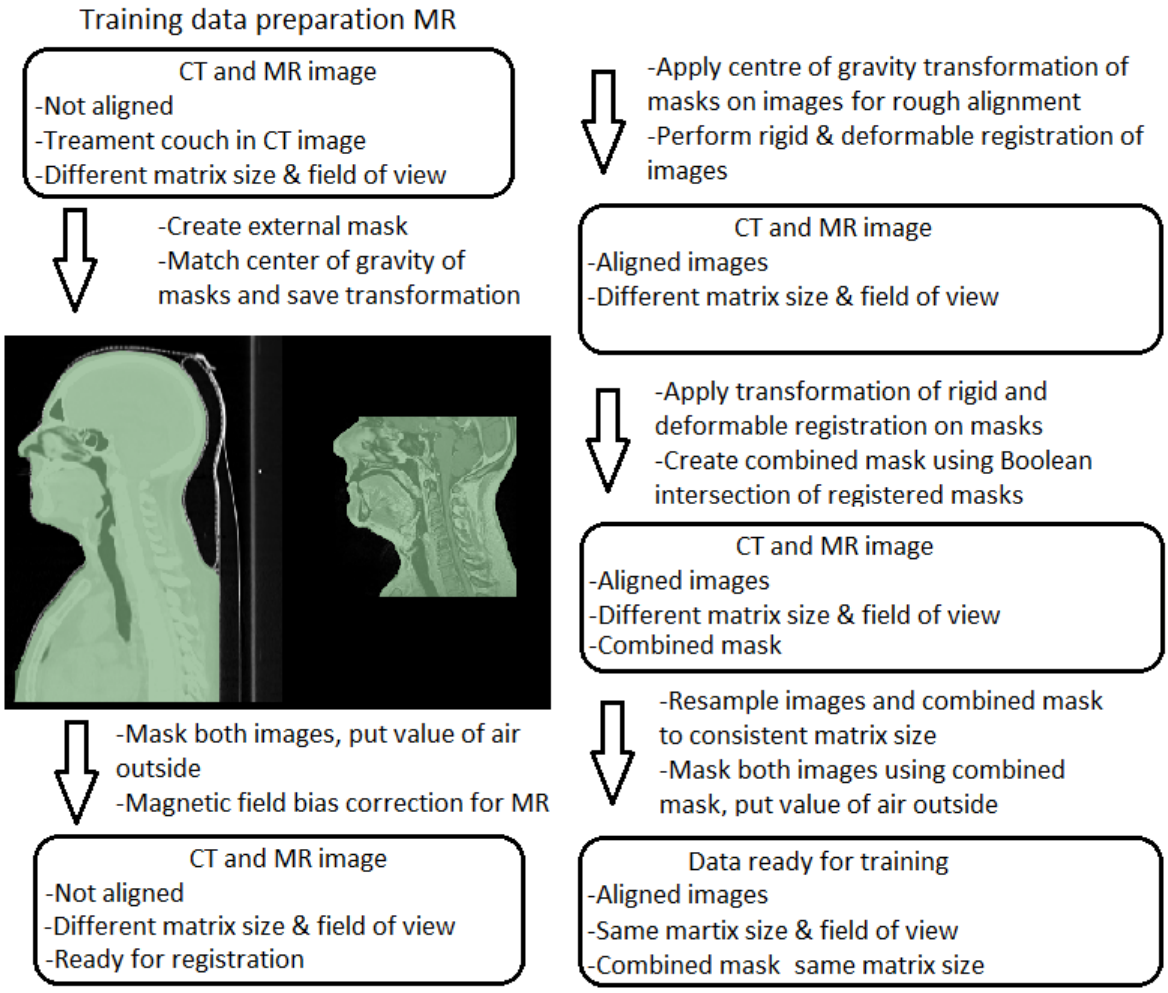

Figure 9: Training data preparation steps MR.

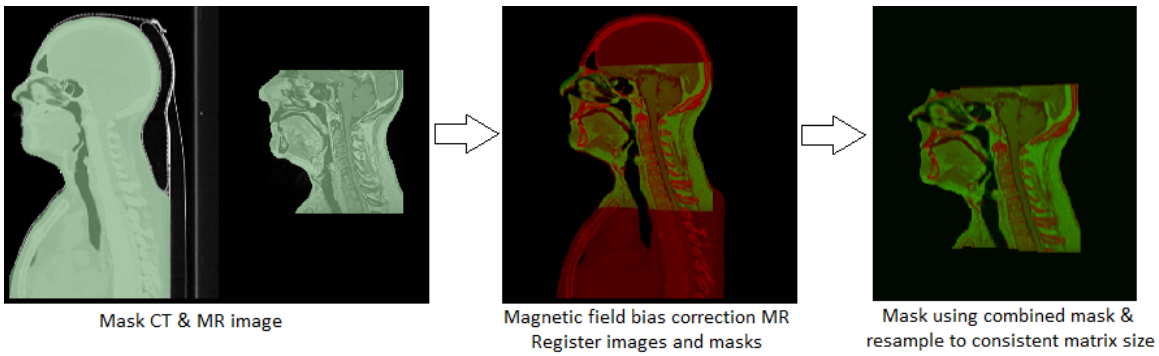

Figure 10: Training data preparation steps MR. From left to right: overlay of external masks on CT and MR image, overlay of registered CT (red) and MR (green) images, overlay of registered CT (red) and MR (green) images masked with combined mask and re-sampled to same matrix size.

2.3.3 Creating fused sCTpCT images

Original clinical treatment plans were based on the pCT images. To be able to make a comparison of dose distributions calculated on the pCT images with those calculated on sCT images based on MR and CBCT images, the sCT images had to be all aligned to the pCT. The CBCT and MR images were rigid and deformable co-registered to the pCT image before they were converted to sCT images by the trained DCNNs.

The CBCT and MR images had a limited FoV compared with the pCT image. Hence, this limitation was still present in the sCT images created from the CBCT and MR images. To decrease the effects of the limited FoV on the dose distribution calculations, the sCT data for the overlapping FoV of the CBCT and MR images was cropped from the sCT images and pasted into the pCT image by performing the following steps.

A mask was made covering the overlapping FoV of the CBCT and MR images. Next, the regions outside the mask in the sCT images and inside the mask in the pCT images were set to zero. Summation of these images was performed to obtain a fused sCTpCT images, an example of fused sCTpCT images is shown in Figure 11. The script used for creating the fused sCTpCT images can be found in appendix A3.

The immobilization mask and patient couch were not taken into account. The couch and immobilization mask were cropped from all images, by setting the voxel values outside an external mask for the pCT to -1000 HU corresponding with the value for air.

To evaluate the precision and accuracy of the fused sCTpCT images used for the dosimetric evaluation, both the MAE and the mean error (ME) were calculated within the overlapping FoV for CBCT and MR images. The ME was calculated using formula (2):

$$ME = \frac{1}{N}\sum^{N}(sCT_{ijk} - CT_{ijk}) \tag{2}$$

in which N is the number of evaluated voxels, sCT_{ijk} and CT_{ijk} are the voxel values at the same position in the image matrix within the sCT and corresponding CT image respectively.

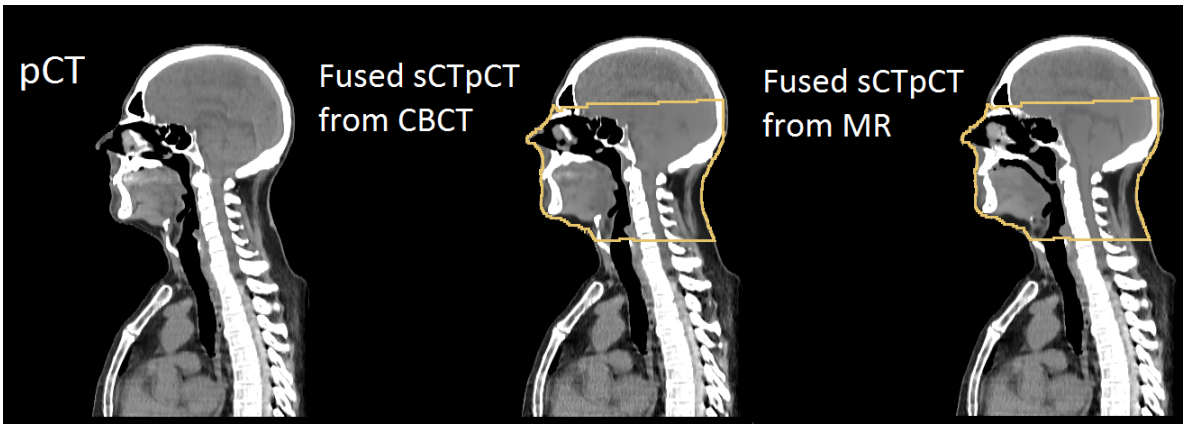

Figure 11: From left to right, pCT, fused sCTpCT image created using sCT based on CBCT image and fused sCTpCT image created using sCT based on MR image. The sCT part of the sCTpCT images can be seen within the ochreous yellow line.

2.4 Dice similarity coefficient

Dice similarity Coefficient (DSC) can be used to asses the geometric similarity of two structures. The DSC is used here to evaluate the geometric accuracy of the reconstruction of bony structures by the DCNN. The DSC is calculated using Formula (3) [65]:

$$DSC = \frac{2(A \bigcap B)}{A + B} \tag{3}$$

In which A and B are the volume of the bony structures in the sCT and pCT images and $A \bigcap B$ is the overlapping volume of the bony structures. DSC values lie between 0 and 1, with 0 indicating no overlap of the strucures and 1 indicating perfect overlap of the structures. A visualization of the DSC can be seen in Figure 12.

The bony structures were segmented from the images by thresholding. Thresholding was done at multiple HU levels of 100 - 1000 HU in steps of 100 HU.

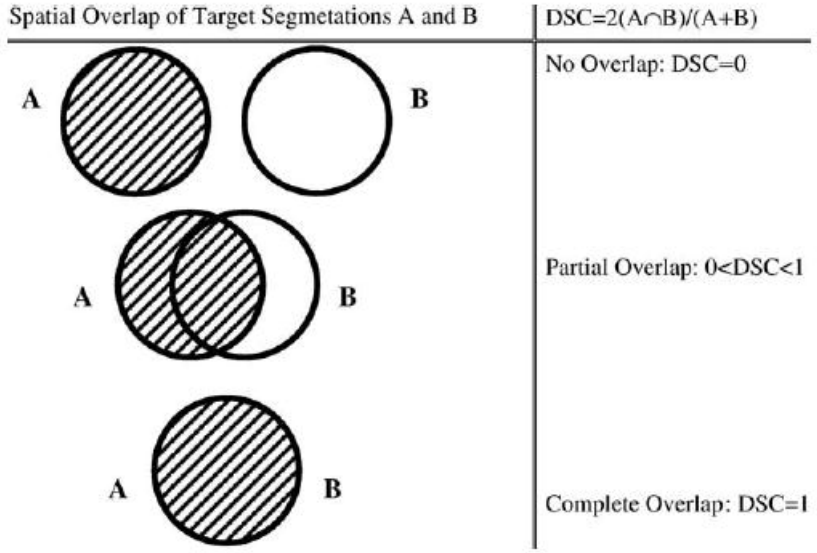

Figure 12: Visualization of DSC [65].

2.5 Dose distribution evaluation

Clinical treatment plans and delineations of target volumes and OARs made by experienced radiotherapy employees were available. Clinical treatment plans had been previously made based on the pCT. Delineations of the planning target volume (PTV), brain stem, parotid glands, mandible and oral cavity were rigidly copied onto the sCT images.

Using the clinical plans, dose distributions were recalculated on the sCT images in RayStation TPS with a dose grid of 0.30X0.30X0.30 cm3. Images of recalculated dose distributions and delineations of OARs can be seen in Figure 13 and 14.

Evaluation of the dose distributions was done using a gamma analysis, using 3% dose difference (DD) and 3 mm distance to agreement (DTA); 2% DD, 2 mm DTA; 1% DD and 1 mm DTA criteria. The gamma analysis was performed using a local 3D gamma analysis algorithm in Plastimatch.

The gamma analysis was performed for the voxels containing sCT data only, in which the dose was above a threshold of 10% of the reference dose. Results of the gamma analysis are reported as the percentage voxels which passed the gamma criteria i.e. gamma index $\gamma(r_R) \leq 1$. The gamma index is calculated with formula 4:[69, 70]

$$\gamma(r_R) = min\{\Gamma(r_R, r_E)\}\forall\{r_E\} \tag{4}$$

in which r_R and r_E are points in the reference and evaluated distribution respectively and $\Gamma(r_R, r_E)$ is calculated using formula 5:

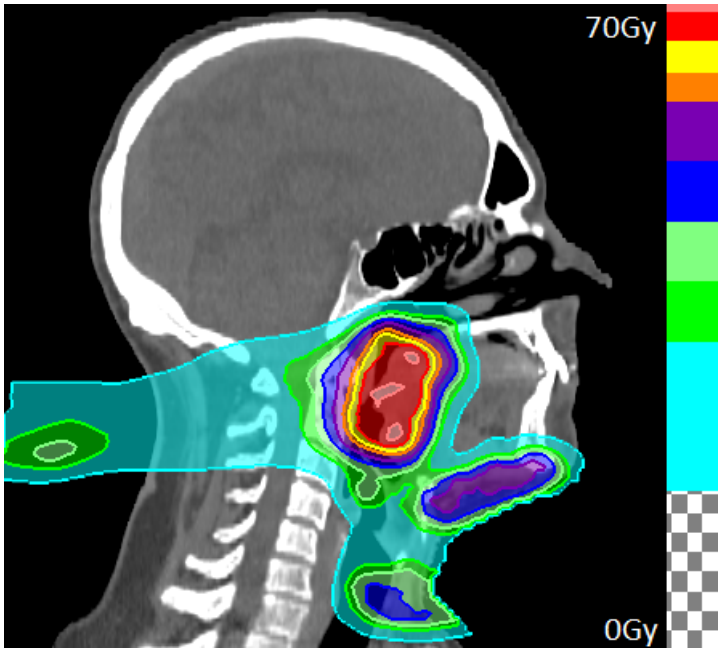

Figure 13: Dose distribution recalculated on pCT image using a clinical proton therapy plan.

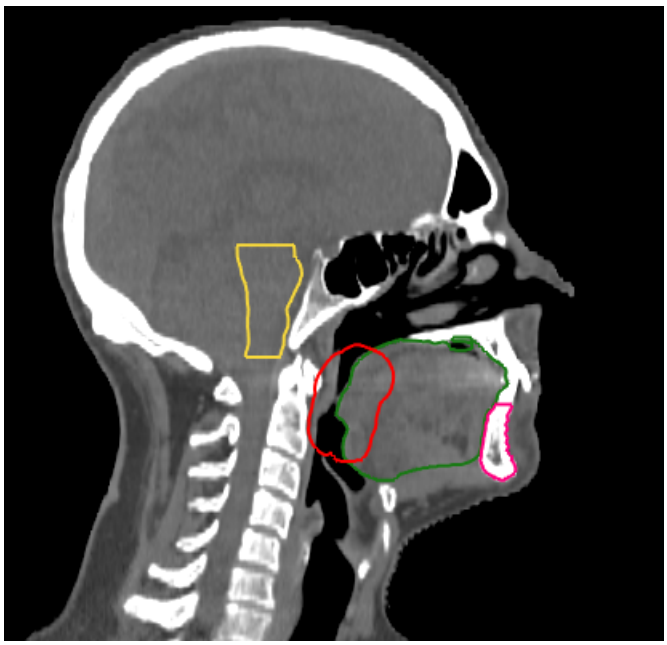

Figure 14: Delineations of OARs, brainstem (yellow), oral cavity (green), PTV (red) and mandible (pink). Left and right parotid glands are not visible in this image slice, but were included in the evaluation.

$$\Gamma(r_R, r_E) = \sqrt{\frac{\Delta r^2(r_R, r_E)}{\delta r^2} + \frac{\Delta D^2(r_R, r_E)}{\delta D^2}} \tag{5}$$

in which Δr is distance between the reference and the evaluated point, ΔD is the dose difference between the reference and evaluated point and δr and δD are the DTA and DD criteria. A graphical visualization of the gamma analysis of a single point is shown in Figure 15. When a evaluated point falls within the circle drawn in the graph of Figure 15, the gamma criteria are fulfilled with respect to the reference point and the point can be marked as passing the gamma criteria [70].

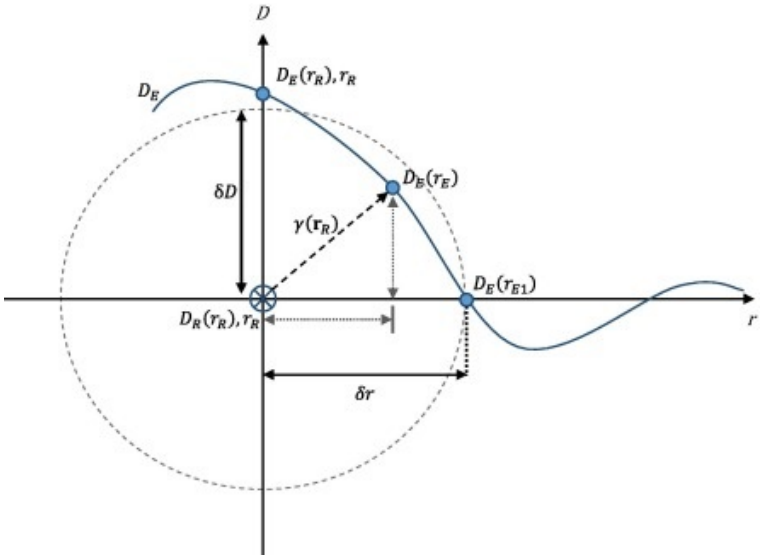

Figure 15: Visualization of gamma analysis [70].

For evaluation of the dose in the OARs, dose volume histograms (DVHs) were constructed for the OARs and certain DVH points were chosen. Some of the by ICRU report 83 recommended DVH points for dose distribution evaluation were chosen [71]. The DVH points which were used, were the maximum dose in 2% of the volume of the OARs ($D_{2\%}$) and the mean dose in the OARs (D_{mean}). Comparing $D_{2\%}$ and D_{mean} evaluated for the dose distributions calculated on the sCT images with those evaluated on a corresponding CT images gives an measure of the accuracy of the calculation of the maximum and mean dose in the OARs.

These chosen DVH points are metrics used in the evaluation and comparison of treatment plans during the treatment planning phase in clinical practice. Furthermore, the minimum dose in 2% ($D_{98\%}$) of PTV was calculated, which gives an impression of the minimum dose planned for a section of the target volume, which is an important DVH point for evaluation of tumor control. The decision to create an adapted plan could for example be triggered, when the clinical target volume, which lies inside the PTV, receives less than 95 % of the planned dose [72].

3 Results

3.1 DCNN training & synthetic CT

Training of the DCNN took 2.5 days on a Nvidia GeForce GTX 1080 Graphics card for a single view. The minimum validation loss was found on average after 18 epochs. Converting CBCT and MR images to sCT images with the trained DCNN took about one minute per patient volume per view. The MAE between the sCT images and pCT images was reduced by combining and averaging the images created for three orthogonal views. A reduction in MAE of about 3 HU and 5 HU for sCT_{CBCT} an sCT_{MR} respectively was achieved, which is about a 10% reduction in MAE for both branches.

The average MAE calculated for nine patients for the CBCT and MR image branch were 37 ± 4 and 58 ± 4 HU respectively. More results of the MAE and ME evaluation of the sCT images can be seen in table 1. A transverse slice of a sCT image and the difference of the sCT with respect to the pCT image for both branches can be seen in Figure 16. In the difference images, a white area can be seen in the brain, representing a low amount of difference between the sCT and pCT images for this area. At the interfaces of structures, more difference can be seen, and these differences are smaller for the images in the CBCT branch than those in the MR branch.

Table 1: MAE and ME results calculated between sCT_{CBCT}, sCT_{MR} and pCT data of nine patients for the CBCT and MR conversion branch.

		Average [HU]	STDEV. [HU]	Range [HU]
sCT_{CBCT}	MAE	37	4	[31.493 - 42.064]
	ME	1	6	[-8.132 - 10.613]
sCT_{MR}	MAE	58	4	[50.894 - 61.485]
	ME	1	8	[-17.716 - 10.616]

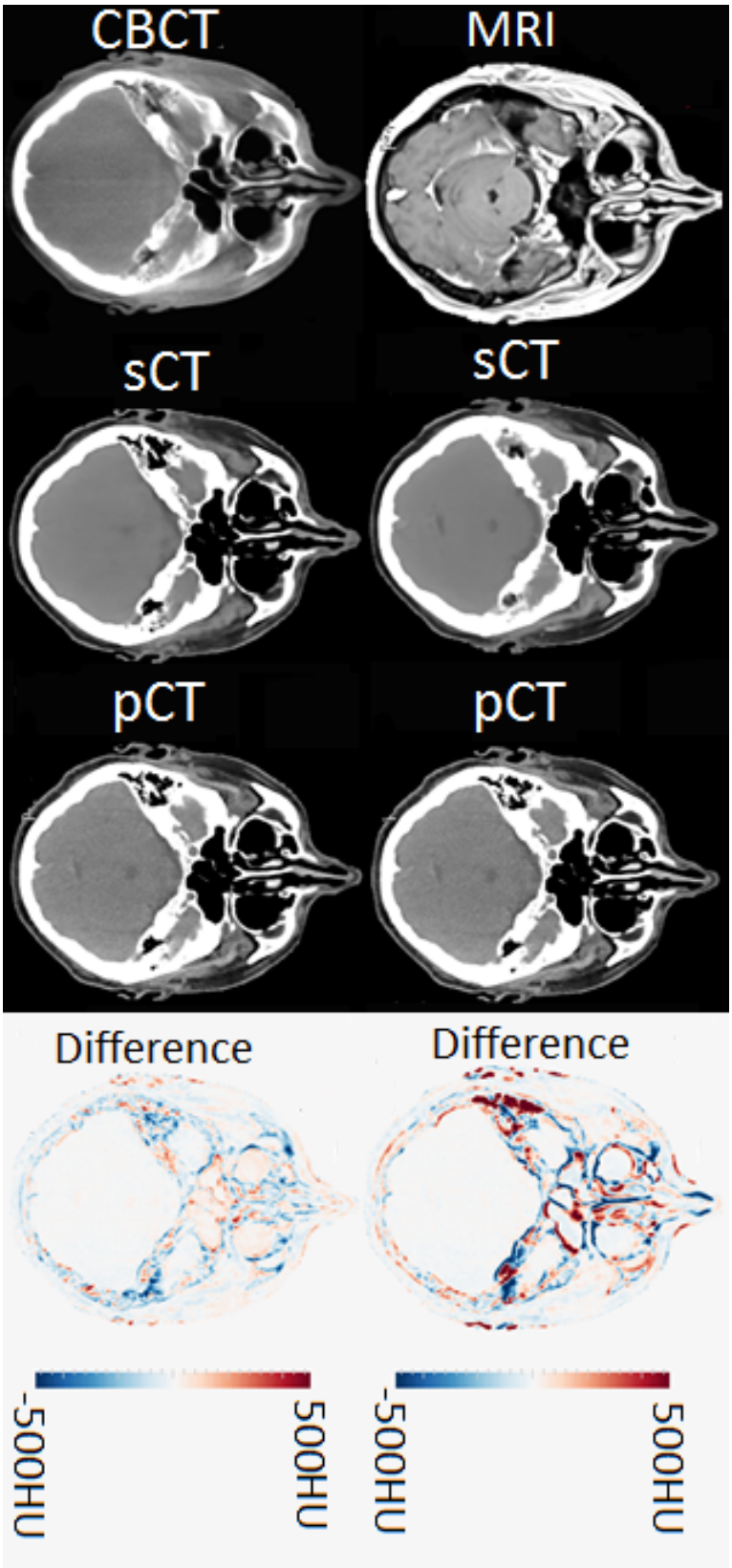

Figure 16: Left column from top to bottom: CBCT, sCT created from CBCT, pCT and difference between sCT created from CBCT and pCT image. Right column from top to bottom: MR, sCT created from MR, pCT and difference between sCT created from MR and pCT image.

The geometric accuracy of the reconstruction of bony structures by the DCNN was evaluated using the DSC. The DSC was calculated for bony structures created by thresholding the sCT and pCT images at multiple HU value thresholds. The sCT an pCT images were thresholded at HU levels of 100 - 1000 HU in steps of 100 HU. The results of the DSC evaluation can be seen in Figure 17. DSC values for bony structures in sCT_{CBCT} images were consistently higher than DSC vales found for the sCT_{MR} images.

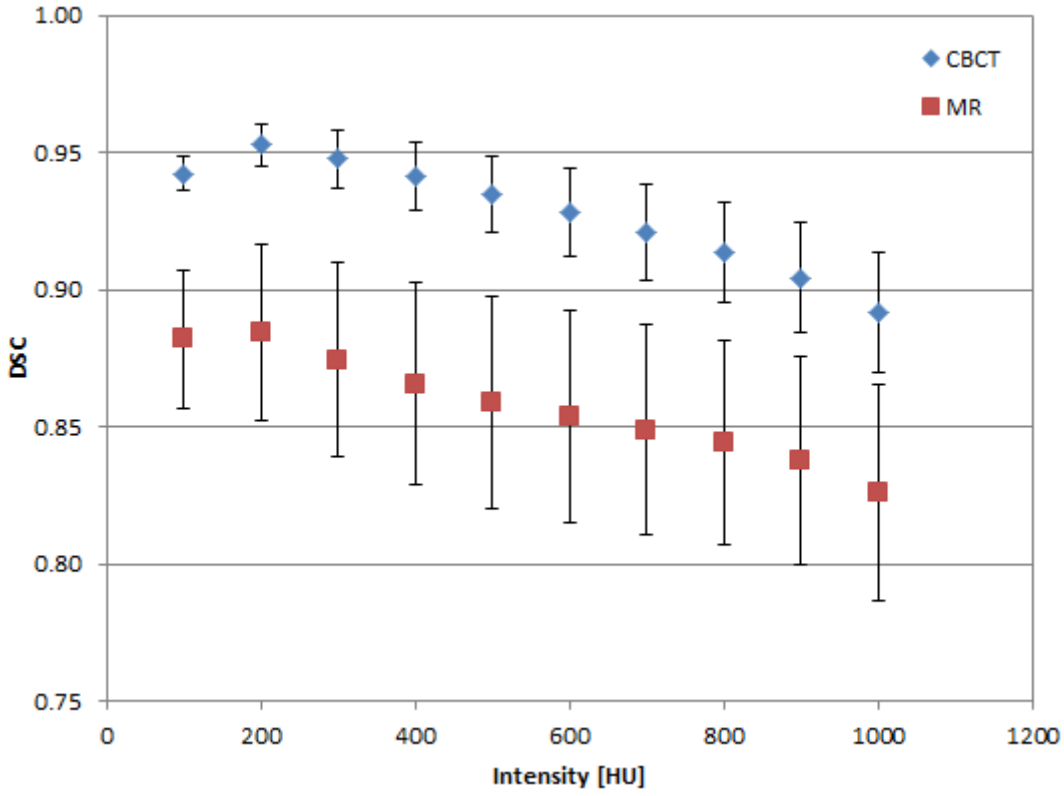

Figure 17: DSC scores as function of the HU value at which the sCT_{CBCT}, sCT_{MR} and pCT images were thresholded.

Scatter plots of MR VS pCT, MR VS sCT, sCT VS pCT and difference between sCT and pCT VS pCT voxel values which occupied the same location in their specific matrix can be seen in Figure 18. Voxels which were within the the external of the patient volume were used, and the amount of data points was decreased by 1/50 to be able to differentiate the data points better. The pearson correlation coefficient (r) for the MR VS pCT was -0.24 indicating a non-linear relationship. Low CT HU values and MR signal is measured for voxels containing air, for which values in the MR VS pCT plot are found at around -1000 HU. High CT HU values and low MR signal are measured for voxels containing bone, for which data points in the MR VS pCT plot are found at around 1000 HU. A pearson correlation coefficient of 0.92 was found between the sCT_{MR} and pCT data, indicating a strong linear relationship between the sCT and pCT data.

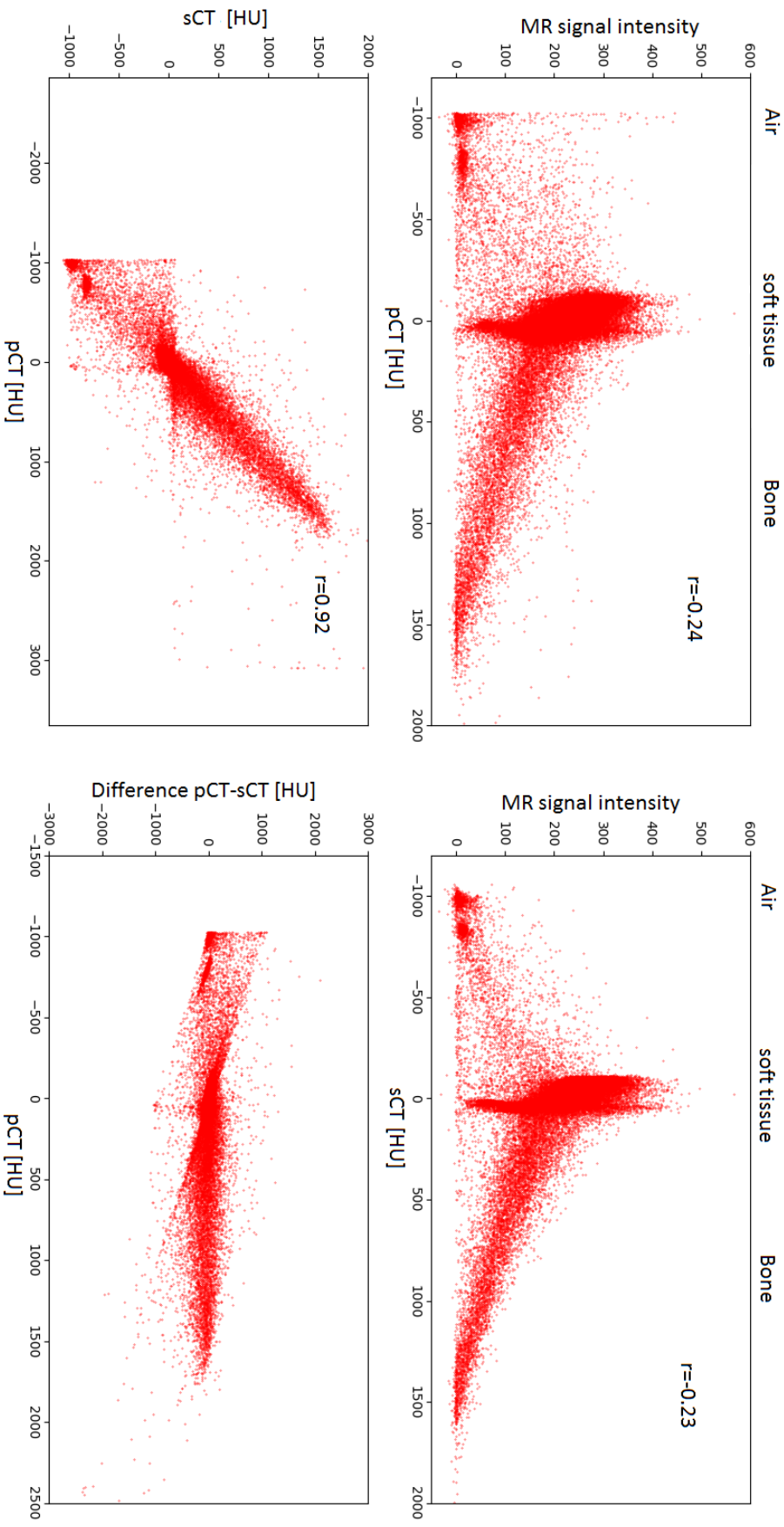

Figure 18: Scatter plots of voxel wise comparison of MR VS pCT top left, MR VS sCT top right, sCT VS pCT bottom left and Difference pCT-sCT VS pCT bottom right.

3.2 Dosimetric evaluation - line dose

A 1D evaluation of the dose distributions was done by plotting the HU and dose values along a line trough the images and dose distributions. The lines were drawn along the coronal and sagittal plain trough the isocenter of the treatment plan for three patients. The used lines can be seen in Figure 19. Plots of the HU and dose values along the lines for the first patient can be seen in Figures 20 and 21. Plots for the second and third patient can be found in appendix C. The dose values along the lines in the sCT dose distributions images closely follow the dose values for the pCT dose distribution.

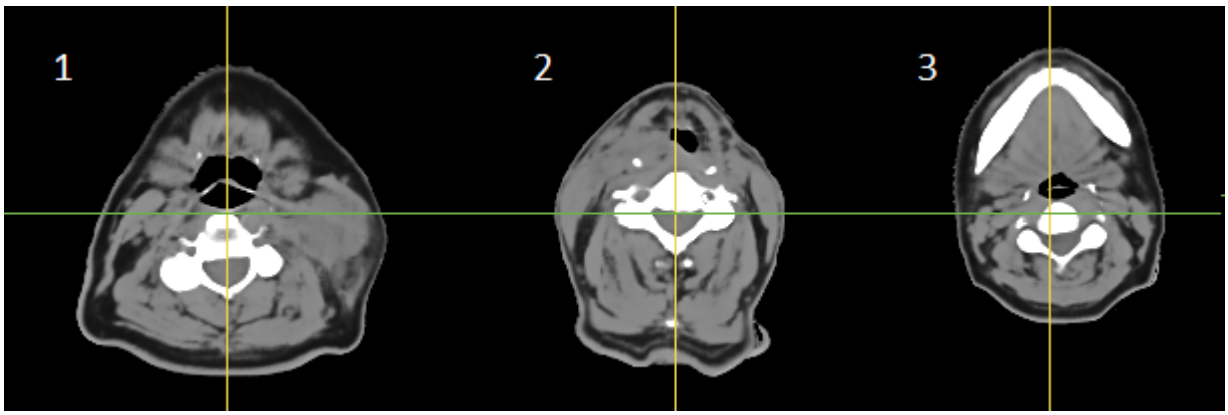

Figure 19: CT images slices of three patients. The isocenter of the treatment plan is at the intersections of the coronal line (green) and sagittal line (yellow). The HU and dose values were evaluated along the coronal and sagittal lines for the patients.

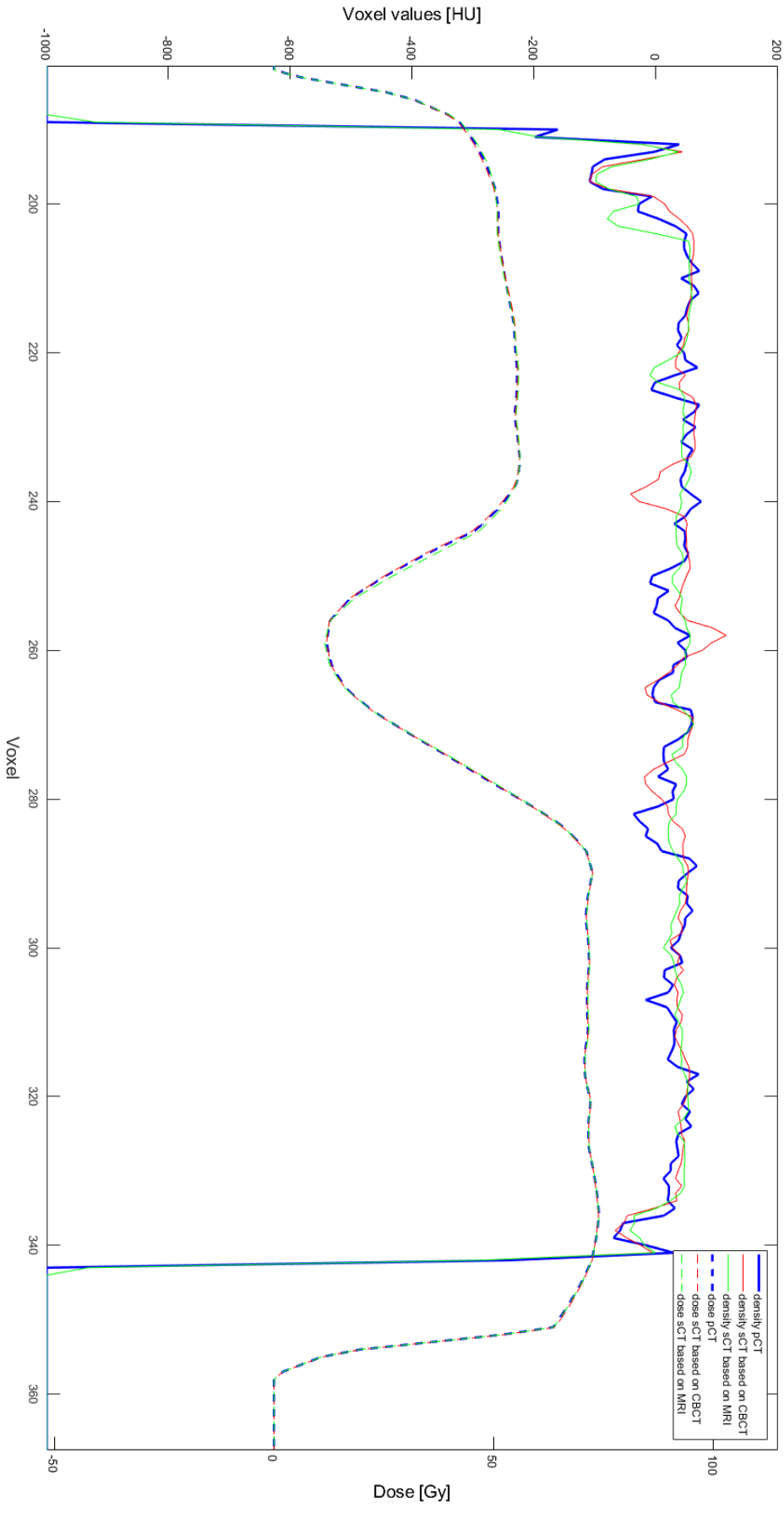

Figure 20: HU and dose values along the coronal line trough the isocenter for pCT, sCT_{CBCT}, sCT_{MR} and corresponding dose distributions of patient 1.

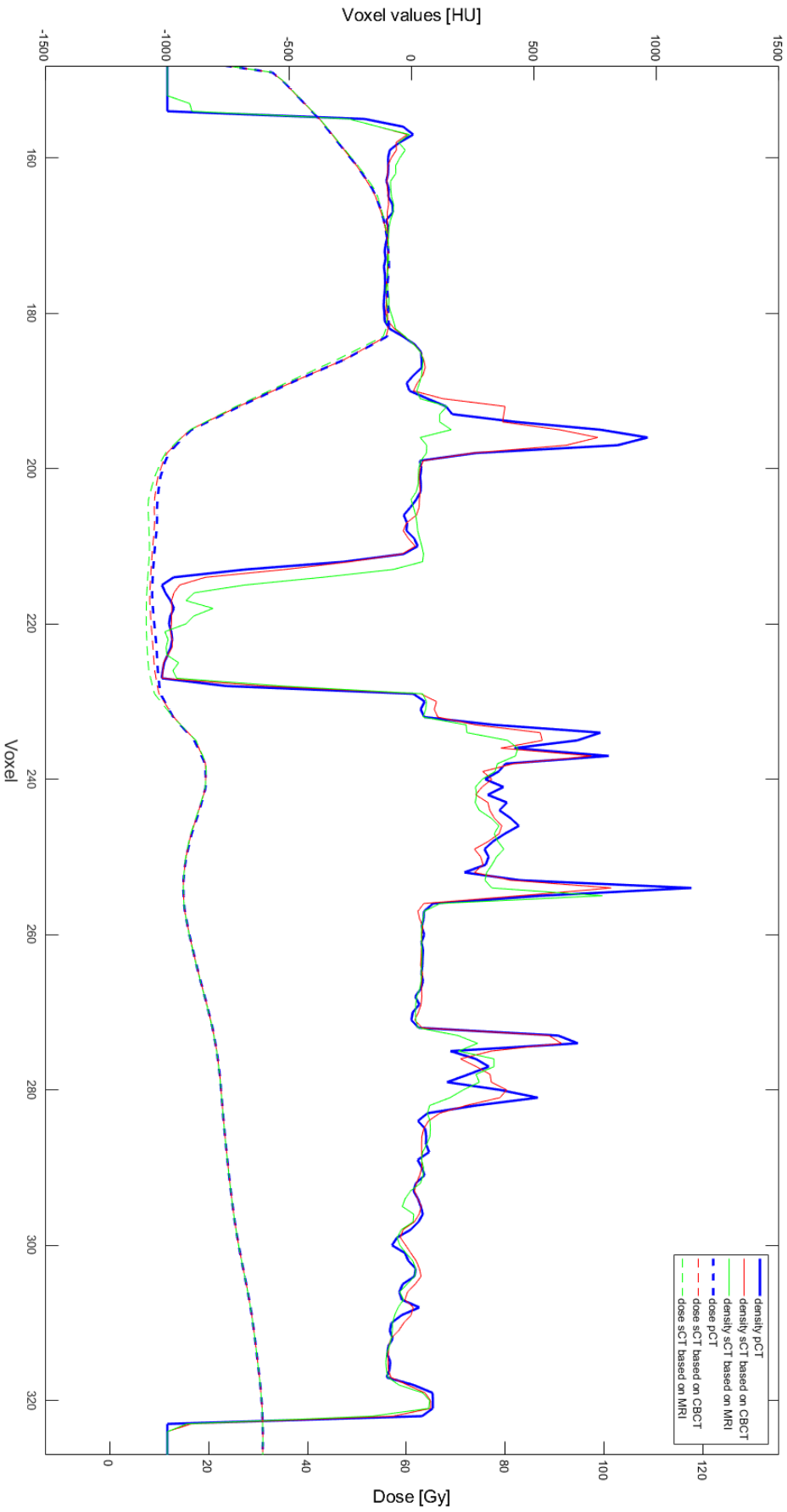

Figure 21: HU and dose values along the sagittal line trough the isocenter for pCT, sCT_{CBCT}, sCT_{MR} and corresponding dose distributions of patient 1.

3.3 Dosimetric evaluation - gamma analysis

A gamma analysis was performed of dose distributions calculated on the fused sCTpCT images compared with original dose distributions calculated on pCT images. The average, standard deviation in the average, maximum and minimum gamma pass rate for 9 patients for 3% DD , 3 mm DTA; 2% DD, 2 mm DTA; 1% DD and 1 mm DTA criteria are reported in table 2. Gamma pass rates determined for all analysed criteria and all patients are reported in table 3.

Table 2: The average, standard deviation in the average, maximum and minimum gamma pass rate for dose distributions calculated on the sCT_{CBCT} and sCT_{MR} images of nine patients for 3% DD , 3 mm DTA; 2% DD, 2 mm DTA; 1% DD and 1 mm DTA criteria.

Criteria	Image	Average [%]	STDEV. [%]	Range [%]
3mm 3%	sCT_{CBCT}	98.6	1.0	[97.3 - 99.7]
	sCT_{MR}	97.5	1.0	[96.1 - 98.9]
2mm 2%	sCT_{CBCT}	97.2	1.5	[94.9 - 99.2]
	sCT_{MR}	95.1	1.5	[93.0 - 97.5]
1mm 1%	sCT_{CBCT}	92.7	2.9	[87.3 - 96.8]
	sCT_{MR}	88.1	2.8	[84.8 - 92.8]

Table 3: Gamma pass rates for dose distributions calculated on the sCT_{CBCT} and sCT_{MR} images of nine patients for 3% DD , 3 mm DTA; 2% DD, 2 mm DTA; 1% DD and 1 mm DTA criteria.

Criteria	Image \Patient #	1[%]	2[%]	3[%]	4[%]	5[%]	6[%]	7[%]	8[%]	9[%]
3mm 3%	sCT_{CBCT}	98	99	99	100	97	98	98	100	98
	sCT_{MR}	97	97	99	98	96	98	97	98	98
2mm 2%	sCT_{CBCT}	96	98	98	99	95	96	97	99	96
	sCT_{MR}	94	95	97	97	93	96	93	95	96
1mm 1%	sCT_{CBCT}	90	94	95	97	87	91	93	95	92
	sCT_{MR}	86	89	93	91	85	89	85	86	89

3.4 Dosimetric evaluation of dose in the target and OARs

Table 4 shows the average D_{mean} for the 9 patients for each OAR. The lowest average D_{mean} with a value of 4.26 Gy was found for the brainstem. Average relative differences in the mean, minimum and maximum dose evaluated in the PTV were less than 0.3% for both the CBCT and MR branch. Average relative differences in the mean and maximum dose in all OARs were less than 1.5% for both the CBCT and MR branch (Table 5). Relative differences in dose at DVH points for target and OARs for the nine separate test patients can be found in appendix D.

Table 4: Avarage D_{mean} calculated on the pCT image, evaluated in OARs for nine head and neck patients.

OAR	Average D_{mean} [Gy]
PTV	71.12
Right Parotid	20.70
Left Parotid	26.43
Brainstem	4.26
Mandible	27.15
Oral Cavity	31.34

Table 5: Avarage, standardeviation in the avarage and range of relative % differences in D_{mean}, $D_{2\%}$ and $D_{98\%}$ evaluated in OARs on for nine head and neck patients.

OAR	Image	DVH Point	Average [%]	STDEV. [%]	Range [%]
PTV	sCT_{CBCT}	D_{mean}	0.037	0.06	[0.00-0.13]
		$D_{98\%}$	0.135	0.16	[0.04-0.26]
		$D_{2\%}$	0.083	0.10	[0.00-0.20]
	sCT_{MR}	D_{mean}	0.080	0.10	[0.01-0.21]
		$D_{98\%}$	0.220	0.22	[0.09-0.38]
		$D_{2\%}$	0.107	0.19	[0.00-0.54]
right parotid	sCT_{CBCT}	D_{mean}	0.502	0.77	[0.00-1.60]
		$D_{2\%}$	0.138	0.20	[0.00-0.47]
	sCT_{MR}	D_{mean}	0.567	0.80	[0.00-1.94]
		$D_{2\%}$	0.229	0.33	[0.00-0.82]
left parotid	sCT_{CBCT}	D_{mean}	0.423	0.76	[0.00-2.93]
		$D_{2\%}$	0.124	0.17	[0.00-0.40]
	sCT_{MR}	D_{mean}	0.669	1.10	[0.00-2.92]
		$D_{2\%}$	0.227	0.28	[0.02-0.49]
Brain stem	sCT_{CBCT}	D_{mean}	0.702	0.94	[0.00-2.72]
		$D_{2\%}$	1.472	1.76	[0.00-3.91]
	sCT_{MR}	D_{mean}	0.549	0.63	[0.00-1.86]
		$D_{2\%}$	0.559	0.75	[0.00-2.14]
Mandible	sCT_{CBCT}	D_{mean}	0.430	0.57	[0.04-2.72]
		$D_{2\%}$	0.099	0.09	[0.01-0.17]
	sCT_{MR}	D_{mean}	0.662	0.90	[0.00-2.15]
		$D_{2\%}$	0.256	0.33	[0.00-0.77]
Oral cavity	sCT_{CBCT}	D_{mean}	0.927	1.17	[0.19-2.83]
		$D_{2\%}$	0.119	0.15	[0.03-0.32]
	sCT_{MR}	D_{mean}	1.223	1.49	[0.11-2.43]
		$D_{2\%}$	0.204	0.28	[0.00-0.50]
All above	sCT_{CBCT}	D_{mean}	0.504		[0.00-2.83]
		$D_{2\%}$	0.339		[0.00-3.91]
	sCT_{MR}	D_{mean}	0.625		[0.00-2.92]
		$D_{2\%}$	0.339		[0.00-2.14]

4 Discussion

In this research the accuracy of proton dose calculations on sCT images created from CBCT and MR images for the use in adaptive proton therapy for head and neck patients is evaluated and compared. The sCT images generated from CBCT and MR images visually resembled their corresponding CT images quite well. Average MEA values of 37 HU and 58 HU for sCT images created from CBCT and MR images respectively are competitive with MAE values found in literature. During this research a paper of researchers from the University Medical Centre Utrecht was published in, which they found a MAE values of 75 ± 9 HU for head and neck patients, using a 3D patch based DCNN approach to generate sCT images based on MR images [73]. For sCT images created using a generative Adversarial Neural Network MAE values for brain radiotherapy patients of 29 ± 5 and 47 ± 11 HU for sCT images based on CBCT and MR respectively [61, 62].

Differences between the sCT images and their corresponding CT images were mainly seen at the interfaces of anatomical structures (see Figure16). The accuracy and precision of converting CBCT and MR images to sCT images using our trained DCNNs, were better for the CBCT branch than for the MR branch. The range in ME and the average in MAE was smaller for the CBCT branch. The worse performance of the DCNN at the interfaces of structures, could have been caused by multiple factors. Imperfections in registration of the training data could have caused the differences at the interfaces. When the images in the training dataset are not perfectly voxel-wise aligned to their corresponding images, voxels at the interface of a tissue air interface, can contain tissue in the CBCT or MR image and air in the corresponding voxel of the CT image. This results in a bad ground truth for the DCNN to learn form at the interfaces of structures.

In Figure 20 the HU values along a line are plotted. It can be noticed that the HU values plotted for the sCT images seem to vary less than HU values of the pCT image. The variation in HU values in the pCT images have been partly caused by image noise. The added contribution of noise for each voxel can not be accurately predicted, since the contribution of noise is random. Because the contribution of noise can not be predicted, it can possibly also not be predicted by the DCNN. Therefore, the absence of the contribution of noise could explain the lower amount of variation in HU values in the sCT images.

During optimization of the registration steps, it was noticed that the performance of the network was strongly dependent on the quality of the registration. If the alignment between the images is off by a few mm the MAE results increased to above 100 HU. Furthermore, The registration of MR images to their corresponding CT images was more challenging than the registration of CBCT images to CT images, which was probably caused by the larger difference in the nature of the signal in MR and CT imaging.

The difference in registration quality of the training data, could have caused difference in performance of the trained DCNNs in creating sCT images based on CBCT and MR images. Another reason for the worse performance of the DCNN at interfaces of struc-

tures could be, that the DCNN is not able to reconstruct structure interfaces with a high enough spatial resolution to capture the large changes in CT HU over small distances at the interfaces. Experiments using a phantom with structures of different sizes could be used to evaluate the spatial resolution of the reconstruction of sCT images by the DCNN.

Differences between the sCT and CT could also be seen at the air cavities in the inner ear, especially in the sCT_{MR} images (see Figure 16). The small structures with bone air interfaces in the inner ear were not well reconstructed. A cause of the poor reconstruction of the inner ear from MR images could be that the MR signal for bone and air is both low and therefore hard to differentiate (see Figure 18). The inaccuracy of the sCT in the inner ear could be taken into account in treatment planning, by not planning beam paths through these poorly reconstructed areas, to reduce the effects these inaccuracies might have on the calculation of the dose distribution.

Deformable registration between the CBCT and MR image and their corresponding CT image was performed for preparation of the data for network training and testing. In deformable registration, information on a local level is matched between the images to generate deformation of the images to get an optimal alignment of the anatomy between the images. It is important to note, that matching of the information between the images does not, per se, mean matching of the anatomy in the images. Especially, this could not be the case in MR to corresponding CT registration, because of the different nature of the MR signal and CT HU measurement and the fact that they do not have a simple linear relationship.

It can be argued that the use of deformable registration, could influence the evaluation of the performance of the DCNN. The sCT images based on the CBCT and MR images are compared with the CT images to which the CBCT and MR images were previously deformable registered. Information had already been matched between the CBCT and MR images and their corresponding CT images in the deformable registration.

In this research we performed visual inspection of all deformable registered images, to make sure the deformation of the images were anatomically realistic and evaluate the alignment of anatomy between the images. To study the performance of the DCNN without the effect of information matching, one could create an experiment in which no deformable registration is necessary by keeping the anatomy and positioning of the anatomy which is scanned in the different imaging modalities constant. Rigid registration based on fiducial markers should then suffice to get sufficient alignment of the anatomy in the images.

When sCT images created by a DCNN are used in a automated adaptive workflow, our data preparation for image conversion needs to be more automated. In our workflow we used external masks by thresholding and performing closing operation on the original image, after which manual filling of residual holes was necessary. To automate the step of creating an external for the patient, a DCNN trained for this image segmentation tasks could possibly be used [74].

Dose distributions were calculated using original clinical plans with multiple beam angles on the sCT_{CBCT} and sCT_{MR} images and their corresponding CT images. Comparison of the dose distributions was done using a gamma analysis and evaluation of the dose in OARs. High gamma pass rates with an average of 98.6% and 97.6% for 3 mm DTA 3% DD criteria, 97.2% and 95.1% for 2 mm DTA 2% DD criteria and 92.7% and 88.1% for 1 mm DTA 1% DD criteria were found for sCT_{CBCT} and sCT_{MR} images respectively. The gamma pass rates we found are comparable with pass rates found by the researchers from Utrecht calculated for photon therapy plans [73].

The high gamma pass rates indicate a good correspondence between the dose distributions calculated on the sCT images compared with dose distributions calculated on the corresponding CT images. The gamma pass rates for each criteria level were higher for dose distributions calculated on the sCT_{CBCT} images than on the sCT_{MR} images, indicating more accurate dose calculations on the sCT_{CBCT} images. This is also which was expected from the better results of sCT generation based on CBCT images.

The average difference between the values of D_{mean}, $D_{2\%}$ and $D_{98\%}$ in the PTV calculated on the sCT images compared with values calculated on the corresponding CT images were less than 0.3% both for sCT images based on CBCT and MR images. The decision to adapt a treatment plan at our department is made based on the dose coverage of the clinical target volume (CTV), which is inside the PTV. The decision to create an adapted plan could for example be triggered by the CTV receiving a less dose than 95% of the planned dose [72]. The small relative dose difference we found for the PTV will not have an significant influence on this decision.

The average difference in mean and maximum dose in most of the other evaluated OARs were below 1%. The dose differences arising from the use of sCT data for dose calculations are smaller than dose differences arising from uncertainties in CT-to-density calibration and the choice of model which is used for dose calculations [75, 76]. Therefore, we conclude that sCT images created by a DCNN from CBCT and MR images are of sufficient quality for the use in adaptive proton therapy for head and neck patients.

In Figure 25 HU and dose values are plotted along a line in the sagittal plane for patient three. A large difference between the HU values in the sCT_{CBCT} compared with HU values of the pCT image can be seen around voxel 230. The line was drawn trough the throat at the hight of the mandible. The large difference could have been caused by a different position of the anatomy in the throat during the acquisition of the CBCT image compared with the position in the pCT image. Also a difference in the dose values around voxels 220 - 230 can be seen for the sCT_{CBCT} dose distribution. The difference in dose could have been caused by the difference of position of the anatomy, which was not aligned by the deformable registration.

The use of sCT images based on CBCT and MR images can make daily evaluation of treatment plans possible for head and neck patients, without a added imaging radiation dose for the patient. Adaptation of the treatment plans for head and neck patients for anatomical changes which occur on the time scale of days does then become feasible.

For the brain stem and the oral cavity larger average relative differences in DVH points were found. The average difference in $D_{2\%}$ of 1.47% was found for the brain stem for sCT_{CBCT} and D_{mean} of 1.22% was found for the oral cavity for sCT_{MR}. The larger relative differences found for the DVH points evaluated in the brain stem, could be explained by the relative lower dose received by the brain stem (see Table4). A lower dose in the brain stem causes that the same difference in dose amounts to a larger *relative* difference in dose.

The larger relative differences found for the DVH points evaluated in the oral cavity, could have been caused by differences in positioning of the tongue, during the acquisition of the CBCT and MR images and with respect to the CT images. By visual inspection, it was noticed that differences in positioning of the tongue was often not completely corrected by deformable registration.

The CBCT and MR images had a limited FoV, hence the sCT images created based on these images inherited the limited FoV. To perform a fair comparison between the performance of the DCNN for converting CBCT and MR images, sCT data was used only of the overlapping FoV of the CBCT and MR images for evaluation. The effect of the limited FoV of the sCT images on the calculation of the dose distributions was minimized by combining the pCT data with the sCT data. This way a full FoV of the upper body was mimicked. The influence of combining the sCT data with data from the pCT images on the evaluation of the dose distributions was minimized by only performing the gamma analysis within the sCT data. Furthermore, it was made sure that the OARs selected for DVH point evaluation were within the sCT FoV. In the future, radiologists could enlarge the field of view of the MR images, when they are to be used for dose calculations.

The ability to perform daily adaptive treatment planning without the burden of an additional radiation dose for the patient could especially be valuable for pediatric patients. pediatric patients have a longer life ahead of them during which they could develop secondary cancers from exposure to radiation [77]. MRI-only workflows using sCT images created from MR images for planning, positioning and treatment plan adaption would be preferred to minimize the imaging dose burden.

Different from adults, children undergo anatomical changes like hardening of the bones [78]. Research should be performed to evaluate if sCT images created from CBCT and MR images for pediatric patients are also of enough quality to perform sufficiently accurate dose calculations.

More research is needed for different regions of the body to evaluate the dosimetric accuracy of the use of sCT images created by a DCNN for the use of adaptive proton therapy. CBCT and MR with corresponding CT data is also available at the department of radiotherapy of the UMCG for low grade glioma patients, breast cancer patients and a limited cohort of paediatric patients. Data for Abdominal pediatric patients could become available in Utrecht.

5 Conclusions

The goal of this research was to evaluate and compare the dosimetric accuracy of the use of sCT images based on CBCT and MR images created by a DCNN for the use of adaptive proton therapy for head and neck cancer patients. From our results it can be concluded that sCT images based on CBCT images were more accurate than than sCT images based on MR images. Dose distributions calculated on sCT images based on CBCT images were more accurate than dose distributions calculated on sCT images based on MR images. Both sCT images based on CBCT and MR images appear to be suitable for the use in adaptive proton therapy for head and neck patients.

6 Research Ethics

6.1 Patient privacy, informed consent and data management.

The use of patient data in research brings up the issues of maintaining privacy of the patients and approval of the patient to use their data is necessary. Image data of previously treated proton therapy patients was used in this research. Patients who get proton therapy are asked if their data can be used for research by use of informed consent forms.

Privacy of the patients was insured by anonymizing the data when the data was downloaded from the radiotherapy patient database [79]. Random patient numbers were given to the patients, only a securely stored excel file contained the information to couple the random numbers to the patients. Furthermore, the data was stored on a drive within the UMCG, the data could not leave the UMCG.

6.2 Collaboration

This research was performed in collaboration with Italian University Magna Gracia. The DCNN which was used for this research was programmed by researchers of Magna Gracia. Paolo Zaffino, Post-doctoral researcher at Magna Gracia, came to Groningen for three weeks to teach us how to train the DCNN and help with data preparation for the DCNN. Furthermore, data preparation of the CBCT images for DCNN training was done by Adrian Thummerer, a PhD student at the department of radiotherapy, a lot of the details of the research were discussed with him. In return, the contribution of Paolo and Adrian to the research will be mentioned, and they will become co-authors if we publish a paper with the results. These arrangements were discussed before the start of the research to give everyone the right expectations.

6.3 Dual use

Use of the results of this research in fields outside the field of adaptive proton therapy could be imagined. For instance, attenuation correction of positron emission tomography

(PET) scans using sCT images derived from MR images using a DCNN could possibly be performed. Conventionally the attenuation correction for PET-scans is done using CT images of the patient [80]. Acquisition of CT scans comes with a dose burden for the patient. The dose burden of the acquisition of CT scans ranges from about 2.1 mSv for head CT scans to about 31 mSv for multiphase abdomen and pelvic CT scans. Estimated is that 1 in 8100 women, who had a routine head CT scan at age 40, will develop cancer from the radiation dose [81].

Integrated PET-MR systems already exist, and the search for accurate PET attenuation correction from MR images is a active field of research [82]. When sCT images derived from MR images are used for attenuation correction, the imaging dose of the acquisition of the CT scan is eliminated. In the former case the dual use of the outcomes of the research would be beneficial.

6.4 Societal impact

The goal of this research was to verify and compare the use of sCT images created from CBCT or MR images by a DCNN for dose calculations for adaptive proton therapy. When sCT images created from CBCT images made for position verification purposes are used for adaptive proton therapy, no rCT images have to be made to evaluate the changes of the patient anatomy. Adaptive proton therapy workflows become more feasible and less expensive, as the workflow with rCT images is more complicated to plan and no rCT image acquisition costs are made. The benefits for society are possibly more frequent use of improved treatment of cancer, using adaptive proton therapy compared with non-adaptive proton therapy. And a reduction of the cost of adaptive proton therapy workflows.

Evaluating the changes in patient anatomy on daily made CBCT or MR images for adaptive proton therapy could reduce the uncertainties in changes in the patient anatomy. Decreasing the uncertainties in changes in the anatomy can lead to the use of smaller planning margins which are needed to account for these uncertainties. The use of smaller planning margins, reduces the dose delivered to healthy tissues surrounding the tumor and thereby, a reduction in side effects of the treatment. Reduced side effects, could decrease the costs of treatment of side effects and the quality of life of the patients after proton therapy is increased.

During conventional adaptive proton therapy, about four rCT images are acquired during the treatment process. Acquisition of these images results in a imaging dose for the patient. Reduction of the imaging dose for the patient is achieved when sCT images created from MR images are used for adaptive proton therapy. The imaging dose might be small compared to the dose received from the therapy, but especially for pediatric patients it is always good to try to reduce dose to healthy tissue on all fronts, as they have a longer life still ahead of them in which they can develop secondary tumors [77].

Acknowledgements

It has been a good time working on this project in collaboration with the researchers of the department and with researchers from the University of Magna Gracia.

First, I would like to thank Assoc. Prof. A.C. Knopf for giving me the opportunity to work on this topic, for her guidance during the project and for the careful reading and checking of the report. It was nice to have weekly meetings to discuss the progress and time management of the project with Antje. The feedback Antje gave on my writing from a early stage of writing the report was very helpful.

Secondly, I would like to thank P. Zaffino for coming to Groningen for three weeks, to teach us how to prepare the data, perform the training of the DCNN and his advice for the research after he had gone back to Italy. And A. Thummerer for the many discussions we had on how to perform the research and his help in preparation of the training data.

Thanks also to dr. ir. A.T.M. Willemsen, for being my mentor during this project, and quick response on emails when I had questions.

I would like to thank dr. R.J.H.M. Steenbakkers for providing the data and discussing the results of the research.

For resolving technical difficulties, installing all needed software, teaching how to use Raystation, good advice for my research and report and good times at the department, I would like to thank Gabriel Guterres Marmitt, Sabine Visser, Hendike Neh, Carmen Seller Oria, Lidia den Otter, Cassia Oraboni Ribeiro, Elske Gort, Lisa van den Bosch, Gijs Katgert, Tiantian Zhai and Erik Bakker.

For providing a good working environment and equipment for the research I would like to thank the department of Radiotherapy of the UMCG, and the staff which made this possible.

Furthermore, I would like to thank my friends and family for their support during my research.

References

[1] Cijfersoverkanker.nl, *https://www.cijfersoverkanker.nl*, IKNL.

[2] T.A. van de Water, H.P. Bijl, C. Schilstra, M. Pijls-Johannesma, J.A. Langendijk, The Potential Benefit of Radiotherapy with Protons in Head and Neck Cancer with Respect to Normal Tissue Sparing: A Systematic Review of Literature, *The Oncologist*, Volume 16, issue 3, March 2011, Pages 366-377

[3] J.K. Kim, J.E. Leeman, N. Riaz, S. McBride, C.J. Tsai, N.Y. Lee, Proton Therapy for Head and Neck Cancer, *Current Treatment Options in Oncology*, Volume 19, issue 6, May 2018

[4] P. Dirix, S. Nuyts, V. van der Poorten, P. Delaere, W. van der Bogeart, The influence of xerostomia after radiotherapy on quality of life, *Supportive Care in Cancer*, Volume 16, issue 2, February 2008, Pages 171-179

[5] B.W. Neville, D.D. Damm, C.M. Allen, E. Jerry, Radiation induces caries, *Oral & maxillofacial pathology*, 2nd edition, 2002, Pages 398-399

[6] A.T. Hara, D.T. Zero, The potential of saliva in protecting against dental erosion, *Monographs in Oral Science*, volume 25, 2014, Pages 197-205

[7] C. Scully, Xerostomia induced burning sensation in the mouth, *Oral and maxillofacial medicine*, 2nd edition, 2008, Pages 79-85

[8] A. Gerbaulet, D. Ash, "Cervix carcinoma", "Prostate cancer", *The GEC ESTRO handbook of brachytherapy*, 2005

[9] J.Buscombe, S. Navalkissoor, Molecular radiotherapy, *Clinical Medicine*, volume 12, issue 4, August 2012, Pages 381-386

[10] M.R. Haymart, M. Banerjee, A.K. Stewart, R.J. Koenig, J.D.Birkmeyer, J.J. Griggs, Use of radioactive iodine for thyroid cancer, *JAMA: The Journal of the American Medical Association*, Volume 306, issue 7, August 2011, Pages 721-728

[11] K.A. Camphausen, L.D. Wagman, R.C. Lawrence, Principles of Radiation Therapy, *Cancer Management: A Multidisciplinary Approach*, 11th edition, 2018

[12] D.S. Chang, F.D. Lasley, I.J. Das, M.S. Mendonca, J.R. Dylancht, Principles of Radiation Therapy, *Basic Radiotherapy Physics and Biology*, 2014, Page 27

[13] E.E. Klein, E.C. Halperin, C.A. Perez, L.W. Brady, "Electron-Beam Therapy: Dosimetry, planning and techniques", *Perez and Brady's Principles and Practice of Radiation Oncology.*, 5th. edition, 2008, Pages 35-37

[14] J.E. Turner, R.N. Hamm, Effects of elastic and inelastic scattering in giving electrons tortuous paths in matter, *Health Physics*, Volume 69, issue 3, Sep 1995, Pages 378-84

[15] Faiz M Khan, Interactions of Ionizing Radiation, *The Physics of Radiation Therapy*, 4th edition, 2009, Pages 54-70

[16] A.R. Smith Proton therapy, *Physics in Medicine & Biology*, volume 51, issue 13, June 2006, Pages 491-504

[17] S. Swisher-McClure, S.M. Hahn, J. Bekelman, Proton beam therapy: the next disruptive innovation in healthcare?, *Postgrad Med J.*, 91(1075), May 2015, Pages 241-243

[18] U. Amaldi, G. Kraft, Radiotherapy with beams of carbon ions, *Reports on Progress in Physics*, volume 68, issue 8, 2005, Pages 1861-1882

[19] F.M Khan, Proton Beam Therapy, *The Physics of Radiation Therapy*, 4th edition, 2009, Pages 515-516

[20] Graph containing dose depth curves, *https://en.wikipedia.org/wiki/Electron_therapy#/media/File:Dose_Depth_Curves.svg*, WikipediA.

[21] X. Tian, K. Liu, Y. Hou, J. Cheng, J. Zhang, The evolution of proton beam therapy: Current and future status, *Molecular and Clinical Oncology*, volume 8, issue 1, 2017, Pages 15-21

[22] R. Miralbell, A. Lomax, L. Cella, U. Schneider. Potential reduction of the incidence of radiation-induced second cancers by using proton beams in the treatment of pediatric tumors, *International Journal of Radiation Oncology Biology Physics*, Volume 54, issue 3, November 2002, Pages 824-829

[23] W. Lui, S.J. Frank, X. Li, Y. Li, P.C. Park, L. Dong, X.R. Zhu, R. Mohan, Effectiveness of robust optimization in intensity-modulated proton therapy planning for head and neck cancers, *Medical Physics*, Volume 40, issue 5, may 2013

[24] W. Lui, R. Mohan, P.C. Park, Z. Lui, H. Li, Y. Li, R. Wu, N. Sahoo, L. Dong, X.R. Zhu, D.R. Grosshans, Dosimetric benefits of robust treatment planning for intensity modulated proton therapy for base-of-skull cancers, *Practical Radiation Oncology*, Volume 4, issue 6, December 2014, Pages 384-391

[25] H. Lu, R. Brett, G. Sharp, S. Safai, S. Jiang, J. Flanz, H. Kooy, A respiratory-gated treatment system for proton therapy, *Medical Physics*, Volume 34, issue 8, August 2007, Pages 3273-3278

[26] J. Yu, S.S. Park, M.G. Herman, K. Langen, M. Mehta, S.J. Feigenberg, Free Breathing versus Breath-Hold Scanning Beam Proton Therapy and Cardiac Sparing in Breast Cancer, *International Journal of Particle Therapy*, Volume 3, issue 3, Winter 2016, Pages 407-413

[27] C.B. Simone, D. Ly, T.D. Dan, J. Ondos, H. Ning, A. Belard, J. O'Connell, R.W. Miller, N.L. Simone, Comparison of intensity-modulated radiotherapy, adaptive radiotherapy, proton radiotherapy, and adaptive proton radiotherapy for treatment of locally advanced head and neck cancer, *Radiotherapy and Oncology*, Volume 101, issue 3, December 2011, Pages 376-382

[28] E.J. Koay, D. Lege, R. Mohan, R. Komaki, J.D. Cox, J.Y. Chang, Adaptive/Non-adaptive Proton Radiation Planning and Outcomes in a Phase II Trial for Locally Advanced Non-small Cell Lung Cancer, *International Journal of Radiation Oncology Biology Physics*, Volume 84, issue 5, December 2012, Pages 1093-1100

[29] M.A. Heesters, H.K. Wijrdeman, H. Struikmans, T. Witkamp, M.A. Moerland, Brain tumor delineation based on CT and MR imaging. Implications for radiotherapy treatment planning, *strahlentherapie und onkologie organ der deutschen röntgengesellschaft*, Volume 169, issue 12, December 1993, Pages 729-33

[30] Y.G. Roussakis, Strategies for adaptive radiotherapy: towards clinically efficient workflows., *University of Birmingham*, Ph.D. Thesis, 2016

[31] J.F. Daisne,M. Sibomana, A. Bol, G. Cosnard, M. Lonneux, V. Grégoire, Evaluation of a multimodality image (CT, MRI and PET) coregistration procedure on phantom and head and neck cancer patients: accuracy, reproducibility and consistency., *Radiotherapy and Oncology*, Volume 69, issue 3, December 2003, Pages 237-245

[32] T. Nyholm, M. Nyberg, M.G. Karlsson, M. Karlsson, Systematisation of spatial uncertainties for comparison between a MR and a CT-based radiotherapy workflow for prostate treatments, *Radiation Oncology*, Volume 54, issue 4, November 2009, Pages 1748-717

[33] P. Alaei, E. Spezi, Imaging dose from cone beam computed tomography in radiation therapy, *Physica medica*, Volume 31, issue 7, November 2015, Pages 647-58

[34] E.K. Hansen, M.K. Bucci, J.M. Quivey, V. Weinberg, P. Xia, Repeat CT imaging and replanning during the course of IMRT for head-and-neck cancer, *International Journal of Radiation Oncology Biology Physics*, Volume 64, issue 2, February 2006, Pages 355-362

[35] L.W. Goldman, Principles of CT: radiation dose and image quality, *Journal of nuclear medicine technology*, Volume 35, issue 4, December 2007, Pages 226-8

[36] B.G. Fallone, B. Murray, S. Rathee, T. Stanescu, S. Steciw, S. Vidakovic, E. Blosser, D. Tymofichuk, First MR images obtained during megavoltage photon irradiation from a prototype integrated linac-MR system, *Medical physics*, Volume 36, issue 6, June 2009, Pages 2084-2088

[37] C. Kontaxis, G.H. Bol, J.J.W. Lagendijk, B.W. Raaymakers, Towards adaptive IMRT sequencing for the MR-linac, *Physics in Medicine & Biology*, Volume 60, issue 6, March 2015, Pages 2493-509

[38] B.M. Oborn, S. Dowdell, P.E. Metcalfe, S. Crozier, R. Mohan, P.J. Keall, Future of medical physics: Real-time MRI-guided proton therapy, *Medical Physics*, Volume 44, issue 8, August 2017, Pages e77-e90

[39] B.W. Raaymakers, A.J.E. Raaijmakers, J.J.W. Lagendijk, Feasibility of MRI guided proton therapy: magnetic field dose effects, *Physics in Medicine & biology*, Volume 53, issue 20, September 2017, Pages 5615-22

[40] S.P. Crijns, B.W. Raaymakers, J.J. Lagendijk, Real-time correction of magnetic field inhomogeneity-induced image distortions for MRI-guided conventional and proton radiotherapy, *Physics in Medicine & biology*, Volume 56, issue 1, Jan 2011, Pages 289-97

[41] C. Rasch, R. Steenbakkers M. van Herk, Target Definition in Prostate, Head, and Neck, *Seminars in Radiation Oncology*, Volume 15, issue 3, July 2005, Pages 136-145

[42] C. Kurz, G. Dedes, A. Resch, M. Reiner, G. Ganswindt, R. Nijhuis, et al. Comparing cone-beam CT intensity correction methods for dose recalculation in adaptive intensity-modulated photon and proton therapy for head and neck cancer, *Acta Oncologica*, Volume 54, issue 9, June 2015, Pages 1651-1657

[43] J.H. Siewerdsen, D.A. Jaffray, Cone-beam computed tomography with a flat-panel imager: magnitude and effects of x-ray scatter, *Medical Physics*, Volume 28, issue 2, 2001, Pages 220-31

[44] I. Fotina, J. Hopfgartner, M. Stock, T. Steininger, C. Lütgendorf-Caucig, D. Georg, Feasibility of CBCT-based dose calculation: comparative analysis of HU adjustment techniques, *Radiotherapy and Oncology*, Volume 104, issue 2, August 2012, Pages 249-256

[45] A.J. den Dekker, J. Sijbers, Data distributions in magnetic resonance images: a review, *Physica Medica*, Volume 30, issue 7, November 2014, Pages 725-741

[46] A. Karotki, K. Mah, G. Meijer, M. Meltsner, Comparison of bulk electron density and voxel-based electron density treatment planning, *Journal of applied clinical Medical Physics*, Volume 12, issue 4, Fall 2011, Pages 97-104

[47] A. Dunlop, D. McQuaid, S. Nill, J. Murray, G. Poludniowski, V.N. Hansen, S. Bhide, C. Nutting, K. Harrington, K. Newbold, U. Oelfke, Comparison of CT number calibration techniques for CBCT-based dose calculation, *Strahlentherapie Und Onkologie*, Volume 191, issue 12, September 2015, Pages 970-978

[48] F. Guerreiro, N. Burgos, A. Dunlop, K. Wongd, I. Petkar, C. Nutting, K. Harrington, S. Bhide, K. Newbold, D. Dearnaley, N.M. de Souza, V.A. Morgan, J. McClelland, S. Nill, M.J. Cardoso, S. Ourselin, U. Oelfke, A.C. Knopf, Evaluation of a multi-atlas CT synthesis approach for MRI-only radiotherapy treatment planning, *Physica Medica*, Volume 35, March 2017, Pages 7-17

[49] A. Dunlop, D. McQuaid, S. Nill, J. Murray, G. Poludniowski, V.N. Hansen, S. Bhide, C. Nutting, K. Harrington, K. Newbold, U. Oelfke, MRI-based treatment planning with pseudo CT generated through atlas registration, *Medical Physics*, Volume 41, issue 5, May 2014, 051711

[50] F. Guerreiro, L. Koivula, E. Seravalli, G.O. Janssens, J.H. Maduro, C.L. Brouwer, E.W. Korevaar, A.C. Knopf, J. Korhonen, B.W. Raaymakers, MRI-based treatment planning with pseudo CT generated through atlas registration, *Physics in Medicine and Biology*, Volume 64, issue 5, Feb 2019, 055010

[51] J.D. Lawson, E. Schreibmann, A.B. Jani, T. Fox, Quantitative evaluation of a cone-beam computed tomography–planning computed tomography deformable image registration method for adaptive radiation therapy, *Journal of applied clinical Medical Physics*, Volume 8, issue 4, Fall 2007, pages 96-113

[52] J.D. Lawson, E. Schreibmann, A.B. Jani, T. Fox, QVoxel-wise uncertainty in CT substitute derived from MRI, *Medical Physics*, Volume 39, issue 6, June 2012, pages 3283-3290

[53] H. Yu, C. Caldwell, J. Balogh, K. Mah, Toward magnetic resonance-only simulation: Segmentation of bone in MR for radiation therapy verification of the head, *International Journal of Radiation Oncology Biology Physics*, Volume 89, issue 3, July 2014, pages 649-657

[54] E. Johnstone, J.J. Wyatt, A.M. Henry, S.C. Short, D. Sebag-Montefiore, L. Murray, C.G. Kelly, H.M. McCallum, R. Speight, Systematic Review of Synthetic Computed Tomography Generation Methodologies for Use in Magnetic Resonance Imaging–Only Radiation Therapy, *International Journal of Radiation Oncology Biology Physics*, Volume 100, issue 1, January 2018, pages 199-217

[55] R. Farjam, N. Tyagi, H. Veeraraghavan, A. Apte, K. Zakian, M.A. Hunt, J.O. Deasy, Multi-atlas approach with local registration goodness weighting for MRI-based electron density mapping of head and neck anatomy, *Medical Physics*, Volume 44, issue 7, June 2017, pages 3706-3717

[56] C.M. Ranka, N.Hünemohra, A.M. Nagel, M.C. Röthke, O. Jäkel, S. Greilich, MRI-based simulation of treatment plans for ion radiotherapy in the brain region, *Radiotherapy and Oncology*, Volume 109, issue 3, December 2013, pages 414-418

[57] U. Sinha, *http://aishack.in/tutorials/image-convolution-examples/*, AIshack.in.

[58] X. Han, MR-based synthetic CT generation using a deep convolutional neural network, *medical physics*, Volume 44 issue 4, april 2017, Pages 1408–1419

[59] M.F. Spadea, G. Pileggi, P. Zaffino, P. Salome, C. Catana, D. Izquierdo-Garcia, F. Amato, J. Seco, Deep Convolution Neural Network (DCNN) multi-plane approach to synthetic CT generation from MR images - application in brain proton therapy, *Radiation Oncology*, In Press, 2 July 2019

[60] F. Guerreiro, N. Burgos, A. Dunlop, K. Wong, I. Petkar, C. Nutting, K. Harrington, S. Bhide, K. Newbold, D. Dearnaley, N.M. deSouza, V.A. Morgan, J. McClelland, S. Nill, M.J. Cardoso, S. Ourselin, U. Oelfke, A.C. Knopf Evaluation of a multi-atlas CT synthesis approach for MRI-only radiotherapy treatment planning, *Physics Medica*, Volume 35, March 2017, Pages 7-17

[61] X. Liang, L. Chen, D. Nguyen, Z. Zhou, X. Gu, M. Yang, J. Wang, S. Jiang, Generating synthesized computed tomography (CT) from cone-beam computed tomography (CBCT) using CycleGAN for adaptive radiation therapy, *Physics in Medicine & Biology*, Volume 64, Number 12, June 2019

[62] S. Kazemifar, S. McGuire, R. Timmerman, Z. Wardak, D. Nguyen, Y. Park, S. Jiang, A. Owrangi, MRI-only brain radiotherapy: Assessing the dosimetric accuracy of synthetic CT images generated using a deep learning approach, *Radiotherapy and Oncology*, Volume 136, July 2019, Pages 56-63

[63] G Landry, C. Hua, Current state and future applications of radiological image guidance for particle therapy, *Medical Physics*, Volume 46, issue 2, January 2019, Pages e1086-e1095

[64] S. Klein, M. Staring, K. Murphy, M.A. Viergever, J.P.W. Pluim, elastix: a toolbox for intensity based medical image registration, *IEEE Transactions on Medical Imaging*, Volume 29, January 2010, Pages 196-205

[65] K.H. Zou, S.K. Warfield, A. Bharatha, C.M.C. Tempany, M. R. Kaus, S. J. Haker, W. M. Wells, F.A. Jolesz, R. Kikinis, Statistical Validation of Image Segmentation Quality Based on a Spatial Overlap Index, *Academic Radiology*, Volume 11, issue 2, 2004, Pages 178-189

[66] D.P. Shamonin, E.E. Bron, B.P.F. Lelieveldt, M. Smits, S. Klein, M. Staring, Fast Parallel Image Registration on CPU and GPU for Diagnostic Classification of Alzheimer's Disease, *Frontiers in Neuroinformatics*, Volume 7, January 2014, Pages 1-15

[67] R. Chuter, R. Prestwich, D. Bird, A. Scarsbrook, J. Sykes, D. Wilson, R. Speight, The use of deformable image registration to integrate diagnostic MRI into the radiotherapy planning pathway for head and neck cancer, *Radiotherapy and Oncology*, Volume 122, issue 2, February 2017, Pages 229-235

[68] P. Viola, W.M. Wells III, Alignment by Maximization of Mutual Information, *International Journal of Computer Vision*, Volume 24, September 1997, Pages 137-154

[69] H. Li, L. Dong, L. Zhang, J.N. Yang, M.T. Gillin, X.R. Zhu, Toward a better understanding of the gamma index: Investigation of parameters with a surface-based distance method, *Medical physics*, volume 38, issue 12, December 2011, Pages 6730-41

[70] M. Hussein, C.H. Clark, A. Nisbet, Challenges in calculation of the gamma index in radiotherapy – Towards good practice, *Physica Medica*, volume 36, April 2017, Pages 1-11

[71] N. Hodapp, The ICRU Report 83: prescribing, recording, and reporting photon-beam intensity-modulated radiation therapy (IMRT), *Strahlentherapie und Onkologie*, volume 188, issue 1, Jan 2012, Pages 97-99

[72] R.Y. Wu, A.Y. Liu, T.T. Sio, P. Blanchard, C. Wages, M.V. Amin, G.B. Gunn, U. Titt, R. Ye, K. Suzuki, M.T. Gillin, X.R. Zhu, R.Mohan, S.J. Frank, Intensity-Modulated Proton TherapyAdaptive Planning for Patients with Oropharyngeal Cancer, *International journal of particle therapy*, volume 4, issue 2, December 2017, pages 26-34

[73] A.M. Dinkla, M.C. Florkow, M. Maspero, M.H.F. Savenije, F. Zijlstra, P.A.H. Doornaert, M. van Stralen, M.E.P. Philippens, C.A.T. van den Berg, P.R. Seevinck, Dosimetric evaluation of synthetic CT for head and neck radiotherapy generated by a patch-based three-dimensional convolutional neural network, *Medical Physics*, June 2019, (Epub ahead of print)

[74] Z. Alom, M. Hasan, C. Yakopcic, T.M. Taha, V.K. Asari, Recurrent Residual Convolutional Neural Network based on U-Net (R2U-Net) for Medical Image Segmentation, *Strahlentherapie und Onkologie*, 1802.06955, February 2018

[75] A.J. Lomax, Intensity modulated proton therapy and its sensitivity to treatment uncertainties 1: the potential effects of calculational uncertainties, *Physics in Medicine & Biology*, volume 53, issue 4, February 2018, pages 1027-42

[76] M. Bongile, K.V. Mugabe, R. Sims, G. Godwin, D. Loria, Modeling and dosimetric performance evaluation of the RayStation treatment planning system, *Journal of applied clinical medical physics*, volume 15, issue 5, September 2014, pages 29-46

[77] M.S. Linet, K. P. Kim, P. Rajaraman, Children's Exposure to Diagnostic Medical Radiation and Cancer Risk: Epidemiologic and Dosimetric Considerations, *Pediatric Radiology*, volume 39, supplement 1, February 2009, pages 4-26

[78] K. Takahashi, Y. Morita, S. Ohshima, S. Izumi, Y. Kubota, A. Horii, Bone Density Development of the Temporal Bone Assessed by Computed Tomography, *Otology & Neurotology*, volume 38, 2017, pages 1445-1449

[79] T. Skripcak, C. Belka, W. Bosch, C. Brink, T. Brunner, V. Budach, D. Büttner, J. Debus, A. Dekker, C. Grau, S. Gulliford, C. Hurkmans, U. Just, M. Krause, P. Lambin, J.A. Langendijk, R. Lewensohn, A. Lühr, P. Maingon, M. Masucci, M. Niyazi, P. Poortmans, M. Simon, H. Schmidberger, E. Spezi, M. Stuschke, V. Valentini, M. Verheij, G. Whitfield, B. Zackrisson, D. Zips, M. Baumann. Creating a data exchange strategy for radiotherapy research: Towards federated databases and anonymised public datasets, *Radiotherapy and Oncology*, volume 113, issue 3, December 2014, pages 303-309

[80] P.E. Kinahan, D.W. Townsend, T. Beyer, D. Sashin, Attenuation correction for a combined 3D PET/CT scanner., *Medical Physics*, volume 25, issue 10, October 1998, pages 2046-53

[81] K. Takahashi, Y. Morita, S. Ohshima, S. Izumi, Y. Kubota, A. Horii, Radiation Dose Associated with Common Computed Tomography Examinations and the Associated Lifetime Attributable Risk of Cancer, *Archives of Internal Medicine*, volume 169, issue 22, December 2009, pages 2078-86

[82] M. Hofmann, B. Pichler, B. Schölkopf, T. Beyer, Towards quantitative PET/MRI: a review of MR-based attenuation correction techniques, *European journal of nuclear medicine and molecular imaging*, volume 169, issue 22, December 2009, pages 2078-2086

A Data processing scripts

A.1 Training data preparation MR script 1

```
'''
This script creates masks for CT and MR images and performs a
center of gravity matching of the masks followed by a rigid registration
This transformation can subsequently be used as rough alignment of images
'''

import os
#define function to create a list of paths to patient folders
def list_folder(folder):
    return [os.path.abspath(i) for i in [f.path for f in os.scandir(folder)
    if f.is_dir()] if 'Mijn' not in i]

#create a list of paths to patient folders
patients_folder = list_folder(r'C:\Users\JongBA\3DMR')

#define the parameters for parmeter file for registration of masks
def generate_init_par_file(path):
    global_section = '''[GLOBAL]
moving=%s
fixed=%s
moving_roi=%s
fixed_roi=%s
img_out=%s
xform_out=%s''' % (os.path.join(path, 'mask_3DMR_in.nrrd'), os.path.join(
    path, 'mask_pCT.nrrd'), os.path.join(path, 'mask_3DMR_in.nrrd'), os.path
    .join(path, 'mask_pCT.nrrd'), os.path.join(path, '
    mask_3DMR_in_tomask_pCT_INIT.nrrd'), os.path.join(path, '3
    DMR_in_topCT_INIT.txt'))

    stages_section='''

[STAGE]
xform=align_center_of_gravity

[STAGE]
xform=translation
impl=plastimatch
res=2 2 1
gridsearch_min_overlap=0.95 0.95 0.95
metric=mse
num_substages=2'''

    with open(os.path.join(path, 'par_INIT_reg_3DMR_in.txt'), 'w') as f:
        f.write(global_section)
        f.write(stages_section)

#for every patient in list of patients create masks for MR and CT image
#for every patient in list of patients perform regisration of masks
for ii, patient_folder in enumerate(patients_folder):
```

```
45      print(patient_folder)
46
47  #generate registration parameter file within patient folder
48      generate_init_par_file(patient_folder)
49
50  #get paths to images in patient folder
51      MR3D = [i for i in list_folder(patient_folder) if 'Gd_in' in i][0]
52      pCT_folder = [i for i in list_folder(os.path.join(patient_folder, 'CT')
        ) if 'pCT' in i][0]
53
54      #Convert MR image from .DCM to .nrrd format
55      MR_conversion_command = 'plastimatch convert --input %s --output-img %s
        ' % (MR3D, os.path.join(patient_folder, '3DMR_in.nrrd'))
56      #print(MR_conversion_command)
57      os.system(MR_conversion_command)
58
59      #Convert pCT image from .DCM to .nrrd format
60      pCT_conversion_command = 'plastimatch convert --input %s --output-img %
        s' % (pCT_folder, os.path.join(patient_folder, 'pCT.nrrd'))
61      #print(pCT_conversion_command)
62      os.system(pCT_conversion_command)
63
64      #Create mask pCT
65      segment_command = 'plastimatch segment --input %s --fill-holes --output
        -img %s' % (os.path.join(patient_folder, 'pCT.nrrd'), os.path.join(
        patient_folder, 'mask_pCT.nrrd'))
66      #print(segment_command)
67      os.system(segment_command)
68
69      #Create mask MR
70      segment_command = 'plastimatch segment --input %s --fill-holes --fill-
        options "6 3 1 2 5 1" --lower-threshold 20 --output-img %s' % (os.path.
        join(patient_folder, '3DMR_in.nrrd'), os.path.join(patient_folder, '
        mask_3DMR_in.nrrd'))
71      #print(segment_command)
72      os.system(segment_command)
73
74      #Crop CT couch from CT image
75      mask_command = 'plastimatch mask --input %s --mask %s --mask-value
        -1000 --output %s' % (os.path.join(patient_folder, 'pCT.nrrd'), os.path.
        join(patient_folder, 'mask_pCT.nrrd'), os.path.join(patient_folder, '
        pCT_masked.nrrd'))
76      #print(mask_command)
77      os.system(mask_command)
78
79      #register masks to get an initial transformation
80      init_register_command = 'plastimatch register %s' % (os.path.join(
        patient_folder, 'par_INIT_reg_3DMR_in.txt'))
81      #print(register_command)
82      os.system(init_register_command)
```

Listing 1: Python example

A.2 Training data preparation MR (bash) script 2

```
#!/bin/bash
'''
This script corrects the MR image for magnetic field bias.
Applies initial transformation on MR image
Performs rigid and deformable deformable registration on CT and MR image
Applies the transforms form registration on the masks and combines them
Resamples the images and mask to the same matrix size
Crops the regions outside the combined mask from the images
'''

#Define patients for which the steps schould be performed
root_folder="/home/bas/3DMR_elastix_7"
patients=(P_002 P_003 P_004 P_010 P_011 P_012 P_013 P_014 P_015 P_016 P_017
    P_018 P_019 P_020 P_021 P_024 P_026 P_028 P_029 P_030 P_031 P_032 P_033
    P_034 P_035 P_037 P_039 P_040 P_043)
slicer_path="/usr/local/share/Slicer-4.10.1-linux-amd64"


for patient in ${patients[*]};
do
  echo "PATIENT ${patient}"
  #define variable containing patient folder path
  patient_folder=${root_folder}/${patient}

  # Corrrect for magnetic field bias
  ${slicer_path}/Slicer --launch "${slicer_path}/lib/Slicer-4.10/cli-
    modules/N4ITKBiasFieldCorrection" ${patient_folder}/3DMR_in.nrrd ${
    patient_folder}/3DMR_in_BIASCORR.nrrd

   # Apply INIT transformation on MR image to get rough alignment
        plastimatch warp --input ${patient_folder}/3DMR_in_BIASCORR.nrrd --
    fixed ${patient_folder}/pCT_masked.nrrd --xf ${patient_folder}/3
    DMR_in_topCT_INIT.tfm --output-img ${patient_folder}/3
    DMR_in_BIASCORR_topCT_INIT.nrrd

   # Apply INIT transformation on manually corrected mask MR
        plastimatch warp --input ${patient_folder}/mask_3DMR_in.nrrd --
    fixed ${patient_folder}/pCT_masked.nrrd --xf ${patient_folder}/3
    DMR_in_topCT_INIT.tfm --output-img ${patient_folder}/
    mask_3DMR_in_tomask_pCT_INIT.nrrd


       # Run Elastix rigid registration & copy and rename result from
    output folder into patient folder
        mkdir ${patient_folder}/elastix_files_rigid
        elastix -f ${patient_folder}/pCT_masked.nrrd -m ${patient_folder}/3
    DMR_in_BIASCORR_topCT_INIT.nrrd -out ${patient_folder}/
    elastix_files_rigid -p elastix_rigid_par.txt
        cp "${patient_folder}/elastix_files_rigid/result.0.nrrd" ${
    patient_folder}/3DMR_in_BCORR_topCT_RIGID.nrrd

```

```
38
39  # Apply rigid transformations on mask_MR
40        cp "${patient_folder}/elastix_files_rigid/TransformParameters.0.txt
    " "${patient_folder}/elastix_files_rigid/TransformParameters.0_NN.txt"
41        sed -i 's/FinalBSplineInterpolationOrder 3/
    FinalBSplineInterpolationOrder 0/g' "${patient_folder}/
    elastix_files_rigid/TransformParameters.0_NN.txt"
42
43        mkdir ${patient_folder}/transformix_files_rigid
44        transformix -in ${patient_folder}/mask_3DMR_in_tomask_pCT_INIT.nrrd
     -out ${patient_folder}/transformix_files_rigid -tp "${patient_folder}/
    elastix_files_rigid/TransformParameters.0_NN.txt"
45        cp ${patient_folder}/transformix_files_rigid/result.nrrd ${
    patient_folder}/mask_3DMR_in_topCT_RIGID.nrrd
46
47  # Run Elastix deformable registration, copy and rename result from output
     folder into patient folder
48  mkdir ${patient_folder}/elastix_files_def
49        elastix -f ${patient_folder}/pCT_masked.nrrd -fMask ${
    patient_folder}/mask_pCT.nrrd -m ${patient_folder}/3
    DMR_in_BCORR_topCT_RIGID.nrrd -mMask ${patient_folder}/
    mask_3DMR_in_topCT_RIGID.nrrd -out ${patient_folder}/elastix_files_def -
    p elastix_def_par_7.txt -threads 1
50  cp "${patient_folder}/elastix_files_def/result.0.nrrd" ${patient_folder
    }/3DMR_in_BCORR_topCT_DEF.nrrd
51
52  # Apply deformable transformations on rigid mask_MR
53  cp "${patient_folder}/elastix_files_def/TransformParameters.0.txt" "${
    patient_folder}/elastix_files_def/TransformParameters.0_NN.txt"
54        sed -i 's/FinalBSplineInterpolationOrder 3/
    FinalBSplineInterpolationOrder 0/g' "${patient_folder}/elastix_files_def
    /TransformParameters.0_NN.txt"
55
56  mkdir ${patient_folder}/transformix_files_def
57  transformix -in ${patient_folder}/mask_3DMR_in_topCT_RIGID.nrrd -out ${
    patient_folder}/transformix_files_def -tp "${patient_folder}/
    elastix_files_def/TransformParameters.0_NN.txt"
58  cp ${patient_folder}/transformix_files_def/result.nrrd ${patient_folder}/
    mask_3DMR_in_topCT_DEF.nrrd
59
60  # Combine masks
61  ~/python_venv/bin/python ~/combine_mask.py ${patient_folder}/mask_pCT.
    nrrd ${patient_folder}/mask_3DMR_in_topCT_DEF.nrrd ${patient_folder}/
    mask_combined.nrrd
62
63  # Resample images
64  plastimatch resample --input ${patient_folder}/pCT_masked.nrrd --dim "512
     512 216" --output ${patient_folder}/pCT_masked_resampled.nrrd
65  plastimatch resample --input ${patient_folder}/3DMR_in_BCORR_topCT_DEF.
    nrrd --dim "512 512 216" --output ${patient_folder}/3
    DMR_in_BCORR_topCT_DEF_resampled.nrrd
66  plastimatch resample --input ${patient_folder}/mask_combined.nrrd --dim "
    512 512 216" --interpolation nn --output ${patient_folder}/
```

```
    mask_combined_resampled.nrrd
67
68  # Mask images by applying combined mask
69  plastimatch mask --input ${patient_folder}/pCT_masked_resampled.nrrd --
      mask ${patient_folder}/mask_combined_resampled.nrrd --mask-value -1000
      --output ${patient_folder}/pCT_masked_resampled_fullymasked.nrrd
70  plastimatch mask --input ${patient_folder}/3
      DMR_in_BCORR_topCT_DEF_resampled.nrrd --mask ${patient_folder}/
      mask_combined_resampled.nrrd --mask-value 0 --output ${patient_folder}/3
      DMR_in_BCORR_topCT_DEF_resampled_fullymasked.nrrd
71
72 done
73
74 echo "DONE!"
```

Listing 2: Python example

A.3 Fused sCTpCT generation script

```
1  import os
2  '''
3  This script resamples the CBCT mask
4  Combines the CBCT mask with a MR mask
5  Pastes the sCT images into the pCT image for the overlapping field of view
       for MR and CBCT
6  Gets image data from original CT image and converts fused sCTpCT image from
       .DCM to .nrrd format
7  '''
8  def list_folder(folder):
9      return [os.path.abspath(i) for i in [f.path for f in os.scandir(folder)
       if f.is_dir()] if 'P_0' in i]
10
11 patients_folder = list_folder(r'Z:\testtest')
12
13 for patient_folder in patients_folder:
14
15   #resample CBCT mask to size of MR mask
16   Resample_mask_CBCT_command= 'plastimatch resample --input %s --dim "512
       512 216" --interpolation nn --output %s' % (os.path.join(patient_folder,
       'mask_CBCT_cropped_registered.nrrd'), os.path.join(patient_folder, '
       mask_CBCT_cropped_registered_resampled.nrrd'))
17   #print(Resample_mask_CBCT_command)
18   os.system(Resample_mask_CBCT_command)
19
20   #Combine masks using boolean intersection
21   Combine_masks_command= 'plastimatch mask --input %s --mask %s --mask-
       value 0 --output %s' % (os.path.join(patient_folder, '
       mask_combined_resampled.nrrd'), os.path.join(patient_folder, '
       mask_CBCT_cropped_registered_resampled.nrrd'), os.path.join(
       patient_folder, 'mask_combined_resampled_3masks.nrrd'))
22   #print(Combine_masks_command)
23   os.system(Combine_masks_command)
24
```

```
25 #Set values outside of combined mask to 0 to prepare for fusion of sCT
     from MR and pCT images
26 Mask_sCTfromMR_command= 'plastimatch mask --input %s --mask %s --mask-
     value 0 --output %s' % (os.path.join(patient_folder, '
     sCT_ax16_sag17_cor25_voted.nrrd'), os.path.join(patient_folder, '
     mask_combined_resampled_3masks.nrrd'), os.path.join(patient_folder, '
     sCT_fromMR_3masked.nrrd'))
27 #print(Mask_sCTfromMR_command)
28 os.system(Mask_sCTfromMR_command)
29
30 #Set values outside of combined mask to 0 to prepare for fusion of sCT
     from CBCT and pCT images
31 Mask_sCTfromCBCT_command= 'plastimatch mask --input %s --mask %s --mask-
     value 0 --output %s' % (os.path.join(patient_folder, '
     sCTCBCT_ax26_sag13_cor19_voted.nrrd'), os.path.join(patient_folder, '
     mask_combined_resampled_3masks.nrrd'), os.path.join(patient_folder, '
     sCT_fromCBCT_3masked.nrrd'))
32 #print(Mask_sCTfromCBCT_command)
33 os.system(Mask_sCTfromCBCT_command)
34
35 #resample sCT from CBCT image to size of mask
36 Resample_sCTfromCBCT_command= 'plastimatch resample --input %s --dim "512
     512 216" --output %s' % (os.path.join(patient_folder, '
     sCT_fromCBCT_3masked.nrrd'), os.path.join(patient_folder, '
     sCT_fromCBCT_3masked_resampled.nrrd'))
37 #print(Mask_sCTfromCBCT_command)
38 os.system(Resample_sCTfromCBCT_command)
39
40 #Set values at location of combined mask to 0 to prepare for fusion of
     sCT and pCT images
41 Prepare_pCT_command= 'plastimatch fill --input %s --mask %s --mask-value
     0 --output %s' % (os.path.join(patient_folder, 'pCT_masked_resampled.
     nrrd'), os.path.join(patient_folder, 'mask_combined_resampled_3masks.
     nrrd'), os.path.join(patient_folder, 'pCT_masked_resampled_3masks.nrrd')
     )
42 #print(Prepare_pCT_command)
43 os.system(Prepare_pCT_command)
44
45 #Add prepared sCT from MR and pCT images to end up with fused sCTpCT
     images
46 fuse_sCTfromMR_pCT_command= 'plastimatch add --output %s %s %s' % (os.
     path.join(patient_folder, 'sCTpCT_fromMR.nrrd'), os.path.join(
     patient_folder, 'pCT_masked_resampled_3masks.nrrd'), os.path.join(
     patient_folder, 'sCT_fromMR_3masked.nrrd'))
47 #print(fuse_sCTfromMR_pCT_command)
48 os.system(fuse_sCTfromMR_pCT_command)
49
50 #Add prepared sCT from CBCT and pCT images to end up with fused sCTpCT
     images
51 fuse_sCTfromCBCT_pCT_command= 'plastimatch add --output %s %s %s' % (os.
     path.join(patient_folder, 'sCTpCT_fromCBCT.nrrd'), os.path.join(
     patient_folder, 'pCT_masked_resampled_3masks.nrrd'), os.path.join(
     patient_folder, 'sCT_fromCBCT_3masked_resampled.nrrd'))
```

```
#print(fuse_sCTfromCBCT_pCT_command)
os.system(fuse_sCTfromCBCT_pCT_command)

#convert sCTpCT fused images to DICOM with original pCT as reference CT for resampling and image information

#get path to original pCT image
#print(os.listdir(patient_folder))
first_folder= [os.path.join(patient_folder, os.path.normpath(d)) for d in os.listdir(patient_folder) if os.path.isdir(os.path.join(patient_folder, d))]
#print("first folder path: ",first_folder[0])
second_folder= os.path.join(first_folder[0], os.path.normpath(os.listdir(first_folder[0])[0]))
#print(second_folder)
list_second_folder= os.listdir(second_folder)
#print(list_second_folder)
pCT_path = os.path.join(second_folder,[i for i in list_second_folder if 'pCT' in i][0])
str1="\""
pCT_path_string= str1 + pCT_path + str1
#print(pCT_path_string)

sCTpCT_fromMR_toDICOM_command= 'plastimatch convert --input %s --fixed %s --referenced-ct %s --output-dicom %s' % (os.path.join(patient_folder, 'sCTpCT_fromMR.nrrd'), os.path.join(patient_folder, 'pCT_masked.nrrd'), pCT_path_string, os.path.join(patient_folder, 'sCTpCT_fromMR_DICOM'))
#print(sCTpCT_toDICOM_command)
os.system(sCTpCT_fromMR_toDICOM_command)

sCTpCT_fromCBCT_toDICOM_command= 'plastimatch convert --input %s --fixed %s --referenced-ct %s --output-dicom %s' % (os.path.join(patient_folder, 'sCTpCT_fromCBCT.nrrd'), os.path.join(patient_folder, 'pCT_masked.nrrd'), pCT_path_string, os.path.join(patient_folder, 'sCTpCT_fromCBCT_DICOM'))
#print(sCTpCT_toDICOM_command)
os.system(sCTpCT_fromCBCT_toDICOM_command)

pCT_masked_toDICOM_command= 'plastimatch convert --input %s --referenced-ct %s --output-dicom %s' % (os.path.join(patient_folder, 'pCT_masked.nrrd'), pCT_path_string, os.path.join(patient_folder, 'pCT_masked_DICOM'))
#print(pCT_masked_toDICOM_command)
os.system(pCT_masked_toDICOM_command)
```

Listing 3: Python example

B Deformable registration MR parameter file Elastix

```
(FixedInternalImagePixelType "float")
(MovingInternalImagePixelType "float")
(FixedImageDimension 3)
(MovingImageDimension 3)
(UseDirectionCosines "true")

// ***************** Main Components **************************

(Registration "MultiMetricMultiResolutionRegistration")
(Interpolator "BSplineInterpolator")
(ResampleInterpolator "FinalBSplineInterpolator")
(Resampler "DefaultResampler")

(FixedImagePyramid "FixedSmoothingImagePyramid")
(MovingImagePyramid "MovingSmoothingImagePyramid")

(Optimizer "AdaptiveStochasticGradientDescent")
(Transform "BSplineTransform")
(Metric "AdvancedMattesMutualInformation" "TransformBendingEnergyPenalty")
(Metric0Weight 1)
(Metric1Weight 600) //

// ***************** Transformation **************************

(GridSpacingSchedule 4 2 1)
(FinalGridSpacingInPhysicalUnits 10)
(HowToCombineTransforms "Compose")

// ****************** Similarity measure *********************

(NumberOfHistogramBins 60) //

// ******************** Multiresolution **********************

(NumberOfResolutions 3)

// ******************* Optimizer ****************************

(MaximumNumberOfIterations 500) //

// **************** Image sampling ***********************
```

```
(NumberOfSpatialSamples 10000) //
(NewSamplesEveryIteration "true")
(ImageSampler "RandomSparseMask")
(SampleRegionSize 40)  //
(UseRandomSampleRegion "true")
(MaximumNumberOfSamplingAttempts 5)
(RequiredRatioOfValidSamples 0.05)

// ************* Interpolation and Resampling ****************

(BSplineInterpolationOrder 1)
(FinalBSplineInterpolationOrder 3)

(ShowExactMetricValue "false")
(WriteTransformParametersEachResolution "true")
(WriteResultImageAfterEachResolution "true")
//(WritePyramidImagesAfterEachResolution "true")

(DefaultPixelValue 0)
(WriteResultImage "true")
(ResultImagePixelType "short")
(ResultImageFormat "nrrd")
```

C Dosimetric evaluation - line dose

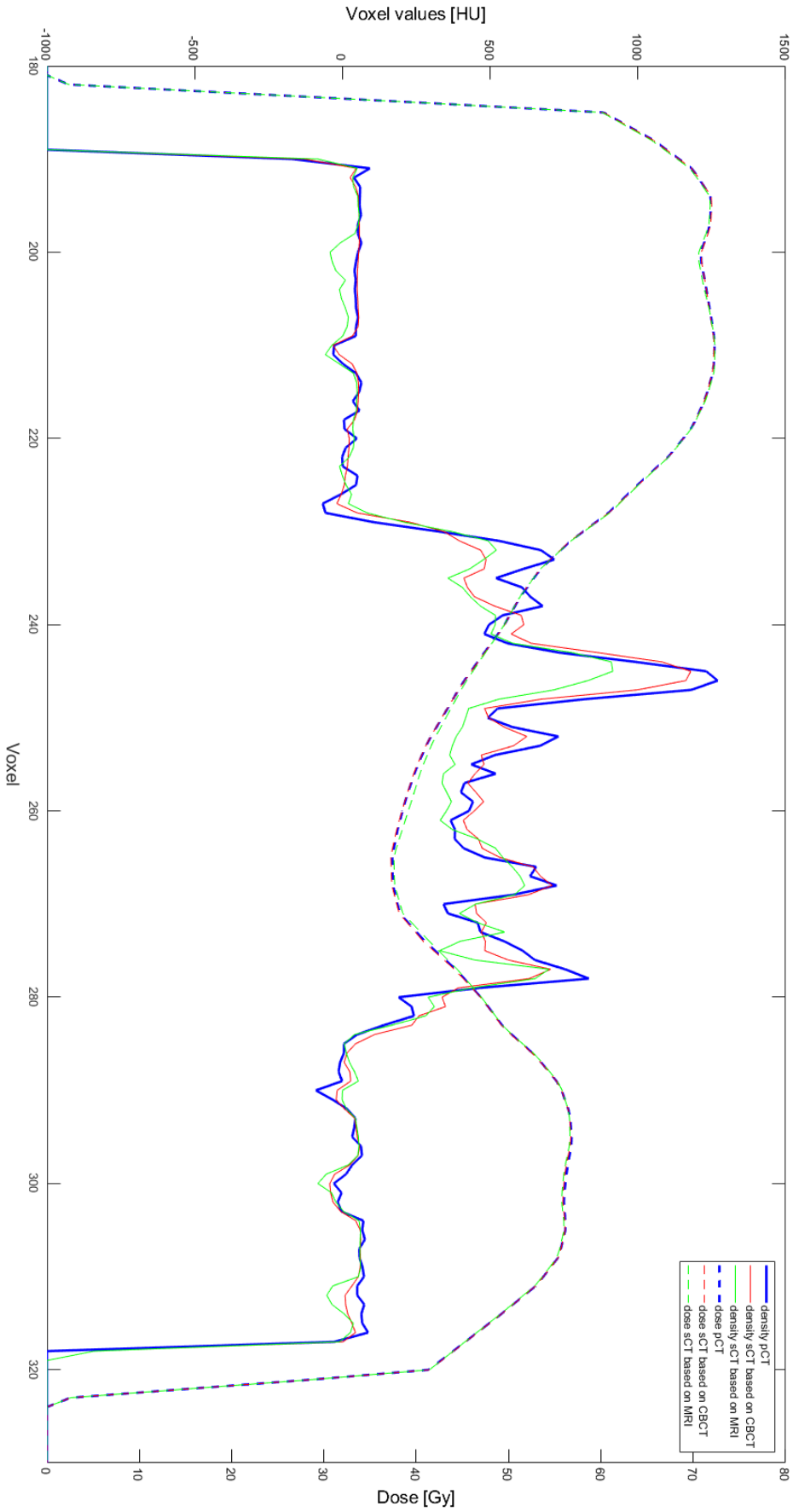

Figure 22: HU and dose values along the coronal line trough the isocenter for pCT, sCT_{CBCT}, sCT_{MR} and corresponding dose distributions of patient 2.

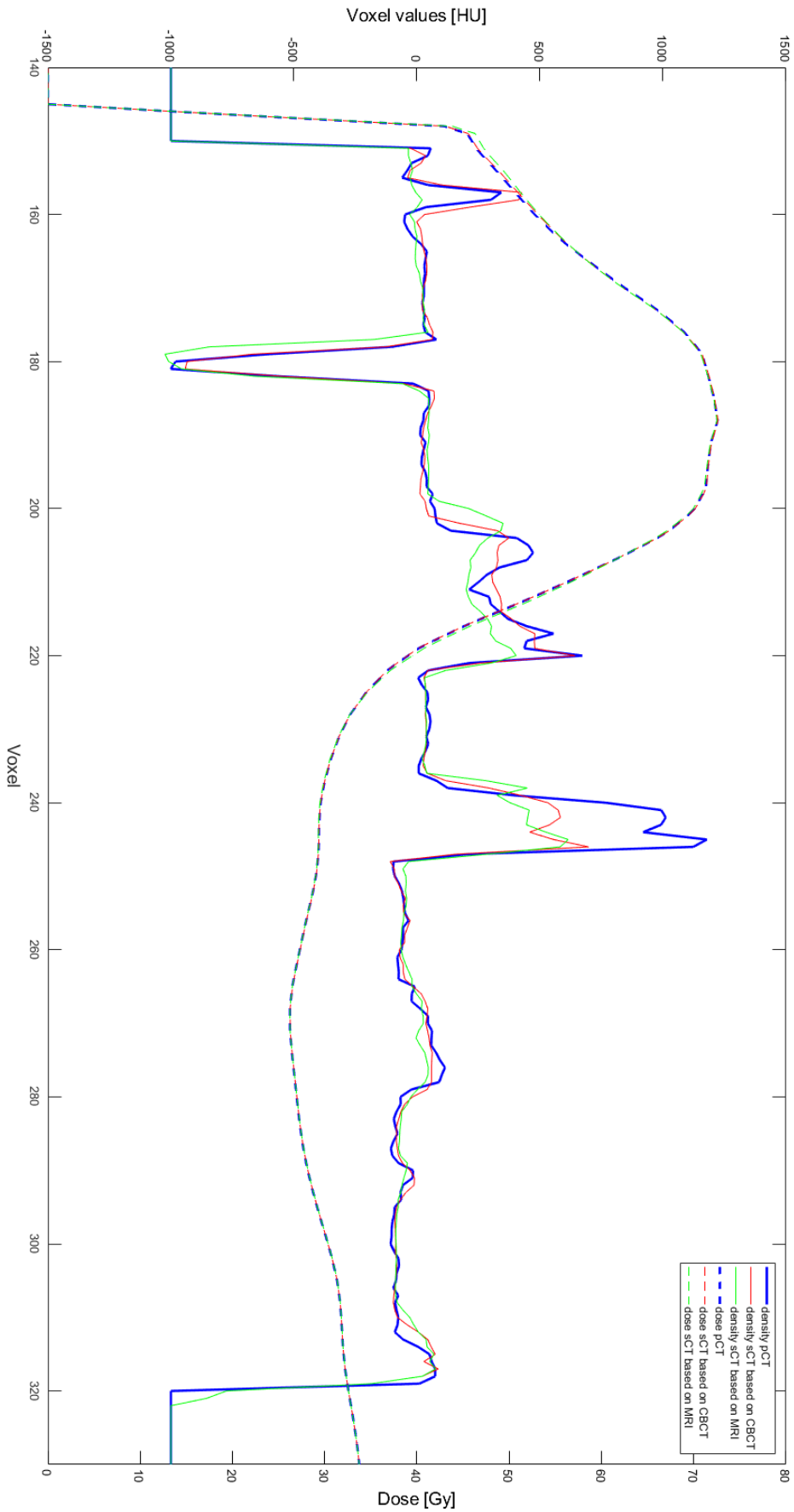

Figure 23: HU and dose values along the sagittal line trough the isocenter for pCT, sCT_{CBCT}, sCT_{MR} and corresponding dose distributions of patient 2.

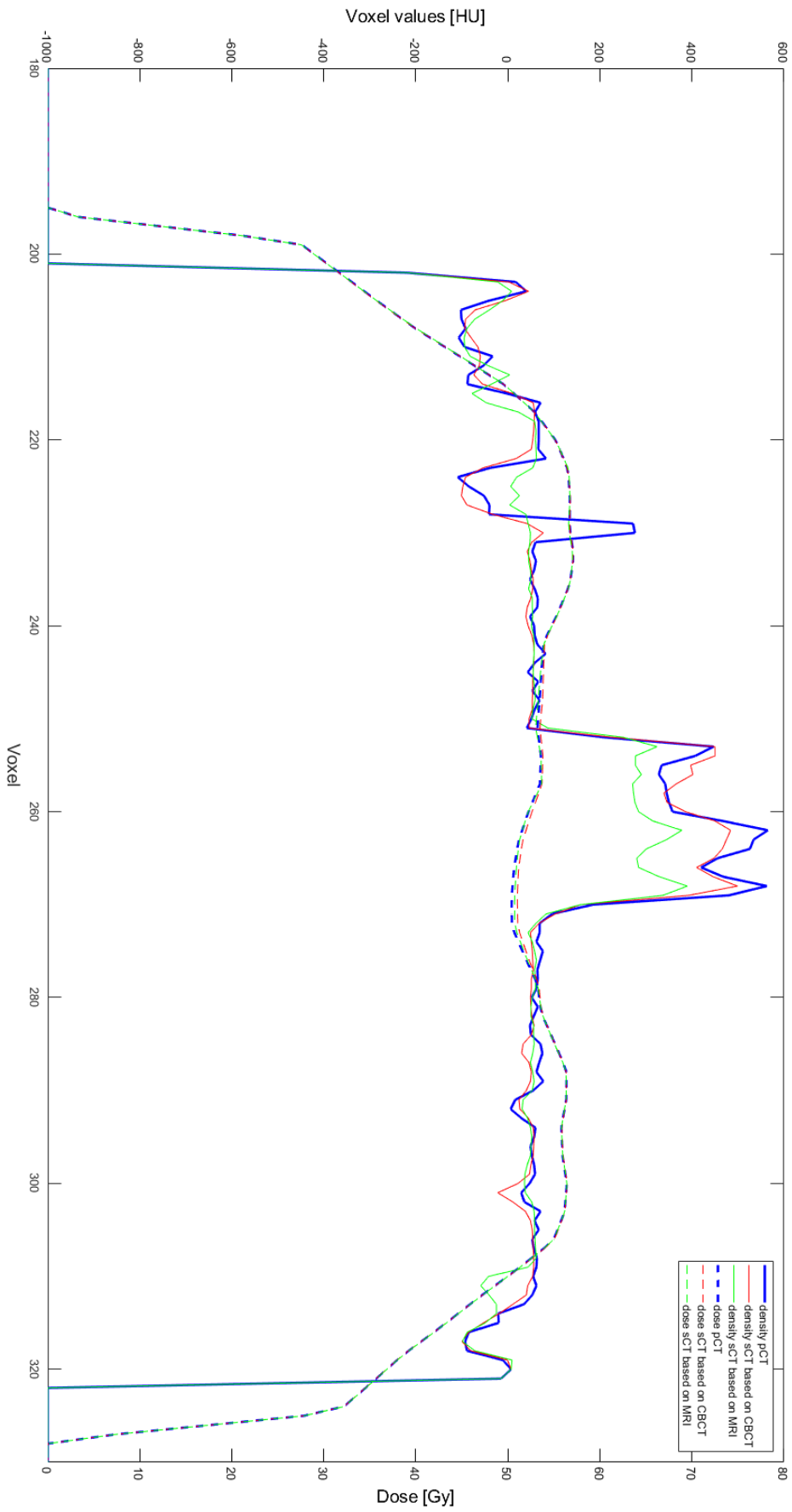

Figure 24: HU and dose values along the coronal line trough the isocenter for pCT, sCT_{CBCT}, sCT_{MR} and corresponding dose distributions of patient 3.

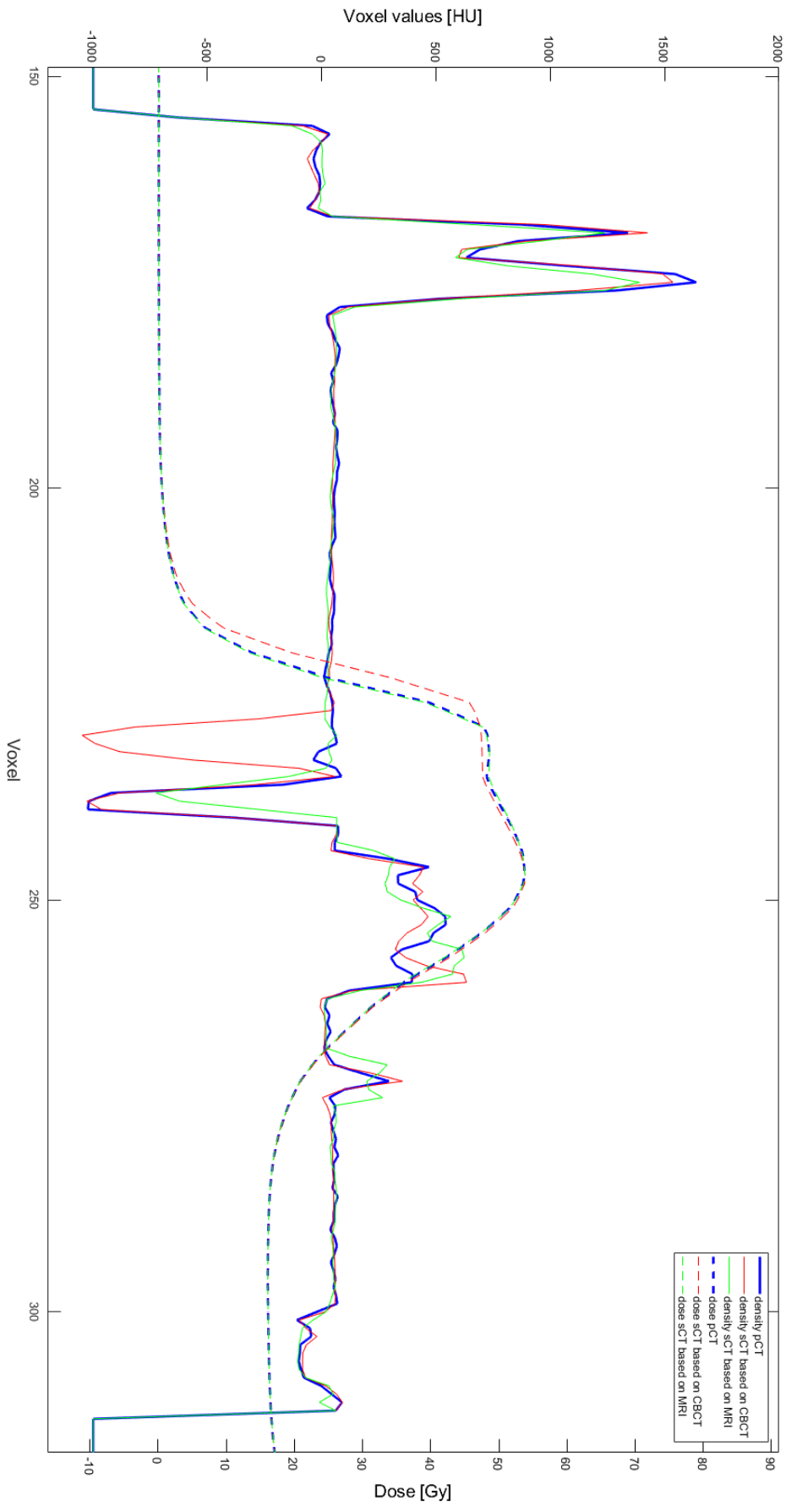

Figure 25: HU and dose values along the sagittal line trough the isocenter for pCT, sCT_{CBCT} sCT_{MR} and corresponding dose distributions of patient 3.

D DVH point evaluation

Table 6: Relative difference in dose at DVH points for target and OARs for dose distribution calculated on sCT_{CBCT} for nine patients.

OAR	DVH point	1[%]	2[%]	3[%]	4[%]	5[%]	6[%]	7[%]	8[%]	9[%]
PTV	$D_{98\%}$	-0,2	-0,2	0,0	0,3	-0,1	-0,1	0,1	0,0	0,2
	D_{mean}	0,0	-0,1	0,1	0,0	0,1	0,0	0,0	0,0	0,0
	$D_{2\%}$	-0,1	-0,1	0,1	-0,1	0,1	-0,2	0,0	-0,1	0,0
Right parotid	D_{mean}	-1,4	0,0	0,4	0,1	-0,1	-0,8	0,0	0,1	1,6
	$D_{2\%}$	-0,3	0,1	0,1	0,0	0,1	0,0	0,0	0,0	0,5
Left parotid	D_{mean}	0,0	-0,4	0,4	0,0	-2,4	-0,3	0,1	-0,2	-0,2
	$D_{2\%}$	0,0	0,1	0,1	0,4	-0,3	0,0	-0,1	0,1	-0,1
Brainstem	D_{mean}	0,6	0,0	-0,8	0,2	-1,0	0,0	-1,0	-2,7	0,0
	$D_{2\%}$	1,1	0,0	-1,1	0,1	-3,4	1,2	-2,4	-3,9	-0,2
Mandible	D_{mean}	0,1	0,4	0,9	-0,3	-1,3	-0,2	0,0	-0,4	0,2
	$D_{2\%}$	0,1	-0,1	0,2	0,2	0,1	0,2	0,0	0,0	0,0
Oral cavity	D_{mean}	-1,9	1,0	0,4	0,5	-0,9	-2,8	-0,3	-0,2	0,4
	$D_{2\%}$	-0,3	-0,1	0,1	-0,3	0,1	0,1	0,0	0,1	0,0%

Table 7: Relative difference in dose at DVH points for target and OARs for dose distribution calculated on sCT_{MR} for nine patients.

OAR	DVH point	1[%]	2[%]	3[%]	4[%]	5[%]	6[%]	7[%]	8[%]	9[%]
PTV	$D_{98\%}$	0,2	-0,2	-0,2	0,2	-0,1	-0,3	0,2	-0,3	-0,4
	D_{mean}	0,1	0,0	0,0	0,0	0,2	-0,1	0,0	-0,1	-0,2
	$D_{2\%}$	0,0	0,0	0,1	-0,1	0,5	0,0	-0,1	0,0	0,0
Right Parotid	D_{mean}	-0,2	0,0	0,5	1,6	-0,4	-0,3	0,0	0,1	1,9
	$D_{2\%}$	0,1	0,0	0,1	-0,8	0,1	0,2	0,0	0,4	0,3
Left Parotid	D_{mean}	0,0	0,0	0,2	0,8	-2,9	0,5	0,1	1,1	0,4
	$D_{2\%}$	0,2	0,0	-0,3	0,5	-0,4	0,1	-0,1	0,3	0,0
Brainstem	D_{mean}	-0,6	0,3	-0,3	-0,1	-0,9	0,0	-1,0	-1,9	0,0
	$D_{2\%}$	-0,1	0,3	-0,5	-0,2	-2,1	0,0	-0,9	0,5	-0,3
Mandible	D_{mean}	0,0	0,3	0,9	2,1	-1,4	-0,2	0,4	0,4	-0,2
	$D_{2\%}$	0,4	0,0	-0,2	0,7	-0,1	0,8	0,0	0,1	0,0
Oral cavity	D_{mean}	-1,1	0,9	2,4	-2,3	-1,4	0,1	2,1	0,5	-0,1
	$D_{2\%}$	0,1	0,1	0,0	-0,4	0,5	-0,2	0,0	-0,5	0,0